Ruprecht-Karls-Universität Heidelberg - Hochschule Heilbronn

Master-Thesis

# Accelerated Quantitative Mapping of Relaxation Times in MRI

UNIVERSITÄT
HEIDELBERG
ZUKUNFT
SEIT 1386

HOCHSCHULE HEILBRONN
TECHNIK WIRTSCHAFT INFORMATIK

SIEMENS


Tom Hilbert
Program of study: MIM
Matriculation number: 177892


| | |
|---|---|
| First Corrector: | Prof. Dr. Rolf Bendl, Universität Heidelberg |
| Second Corrector: | Dr. Gunnar Krüger, Siemens Schweiz AG |
| Supervisor: | Dr. Tobias Kober, Siemens Schweiz AG |

## Abstract

Clinical diagnosis ideally relies on quantitative measures of disease. For a number of diseases, diagnostic guidelines require or at least recommend neuroimaging exams to support the clinical findings. As such, there is also an increasing interest to derive quantitative results from magnetic resonance imaging (MRI) examinations, i.e. images providing quantitative T1, T2, T2* tissue parameters.

Quantitative MRI protocols, however, often require prohibitive long acquisition times ($>$ 10 minutes), nor standards have been established to regulate and control MRI-based quantification.

This work aims at exploring the technical feasibility to accelerate existing MRI acquisition schemes to enable a -3 minutes clinical imaging protocol of quantitative tissue parameters such as T2 and T2* and at identifying technical factors that are key elements to obtain accurate results.

In the first part of this thesis, the signal model of an existing quantitative T2-mapping algorithm is expanded to explore the methodology for a broader use including the application to T2* and its use in the presence of imperfect imaging conditions and system related limitations of the acquisition process.

The second part of this thesis is dedicated to optimize the iterative mapping algorithm for a robust clinical application including the integration on a clinical MR platform. This translation of technology is a major step to enable and validate such new methodology in a realistic clinical environment. The robustness and accuracy of the developed and implemented model is investigated by comparing with the "gold standard" information from fully sampled phantom and in-vivo MRI data.

## Declaration of Authenticity

I submit this work as thesis for my Master of Science at the University Heidelberg and University of Applied Science Heilbronn. It describes my work from the 1st of October 2012 to the 31st of march 2013, in the Advanced Imaging Technology group of Siemens Schweiz AG, located at the École Polytechnique Fédérale de Lausanne. I declare that the work described is my original contribution to the field. Foundation laid by others upon which my work is built have been correctly cited and referenced according to my best knowledge.

Tom Hilbert

## Acknowledgements

I have had the great honour of being supervised by Gunnar Krueger and Tobias Kober. Thank you for the support and great ideas which are the foundation of this project. You both pushed me in the right directions and contributed tremendously to this thesis.

I wish to express my sincere gratitude to Prof. Rolf Bendl for the guidance and providing me an opportunity to write this thesis in collaboration with the Advanced Imaging Technology group of Siemens Schweiz AG.

I would like to gratefully acknowledge the helpful comments and time consuming proof reading of Liliana Caldeira and my brother Marc. Your different point of view helped me to bring this thesis in shape.

Thank you Kieran O'Brian for all the tips and tricks in basic MR physics and optimization problems you taught me during our coffee breaks.

Furthermore, I am grateful to Esen Filiz for motivating and encouraging me especially in difficult and stressful times.

Last but not least, thank you Chemseddine Fatnassi, Maryna Babayeva, Pavel Falkovskiy and colleagues of CIBM for the great collaboration and numerous stimulating discussions. It is a pleasure working with you.

# Contents

# List of Figures

# List of Tables

# 1 Introduction

Magnetic Resonance Imaging (MRI) is a powerful technique in modern medicine. Its good soft tissue contrast offers opportunities to complement the power of Computed Tomography (CT), especially in neuro- and musculoskeletal applications. Advanced techniques, such as diffusion tensor imaging (DTI), arterial spin labelling (ASL), functional MRI (fMRI), Spectroscopy (MRS) and time of flight angiography (TOF-MRA), enhance the image information, hence improving diagnostics of brain diseases, musculoskeletal and other body applications.

However, MRI is a time consuming and cost intensive modality [39]. Physical restrictions lead to long measurement times, for example in comparison to CT. Currently, a large fraction of MR research is focused on speeding up acquisitions using novel reconstruction algorithms. First, speeding up the acquisition will unburden the patient, thus may reduce the probability of motion-artifacts, especially in paediatrics. Second, real-time acquisitions, for example in cardiac-imaging [28] or speech analysis [29] require a good temporal resolution. Finally, MRI requires expensive equipment and supplies, causing high investment and service costs [39]. Therefore, decreasing acquisition times increases the patient throughput, hence improving the cost-effectiveness of the scanner.

MRI data is sampled in Fourier space and thus the Nyquist law of sampling has to be obeyed. In the past, several methods have been developed to speed up acquisitions by measuring less data, thus under-sampling k-space. However, imaging in a sub-Nyquist regime requires novel reconstruction algorithms to recover missing data. These methods are, for example, parallel-imaging, compressed sensing and iterative model-based reconstruction which will be described briefly in the following paragraphs.

Parallel imaging reconstruction is based on reconstructing the image using the under-sampled signal simultaneously measured by multiple receiver coils. Thereby, the feasibility to highly under-sample depends on the number of available coil-elements. In clinical settings, well established methods are Sensitivity Encoding (SENSE)[33] and Generalized Autocalibrating Partially Parallel Acquisitions (GRAPPA)[16].

Compressed sensing is a novel technique introduced in signal processing by Donoho in 2004 [6]. This method assumes that the measured object has a sparse representation in some orthonormal basis such as wavelet or Fourier, meaning the information can be reconstructed on a subset of the most important coefficients. Lustig et al. proposed the application of compressed sensing in MRI [23].

Model-based iterative reconstruction uses prior knowledge about the modulation of the sampled signal and iterative optimization algorithms to reconstruct the image. Thereby, the signal can be mathematically described by a set of parameters. These parameters

depend on tissue properties, namely the proton density and relaxation behaviour. Reconstructing these parameters in spatial maps is defined as quantitative mapping in this work. The potential benefit of quantitative mapping is the comparability intra- and inter-patient. The standard approach to reconstruct quantitative maps is a pixel-by-pixel fitting, which fails when operating on an under-sampled dataset.

The domain of quantitative mapping in MRI is newly formed and needs to be explored in clinical studies: For example, studies to understand the pathophysiology of neurodegenerative disease, by investigating brain iron content [30] using quantitative T2*-maps, or the study to understand white matter (WM) signal abnormalities observed in T2-weighted MRI scans in pre-term infants, which might be caused by developmental stage or diffuse micro-structural white matter abnormalities [19]. This study uses quantitative T2-mapping to be independent from field-inhomogeneities and susceptibility. Moreover, studies to build up knowledge of normative ranges of relaxometry-values are important. For example a study to investigate T1 and T2 relaxation in neonatal brain, the relationship between these rates and their potential use for gray matter (GM) and WM discrimination [43]. However, these studies are rare due to the long acquisition times, usually associated with these measurements. Therefore, decreasing the acquisition time using model-based iterative reconstruction will encourage clinicians to further investigate quantitative mapping.

## 1.1 Goal of this Work

To explore in more detail the potential of model-based iterative reconstruction in the light of acceleration of quantitative imaging procedures the present thesis has the following three goals: 1) extent the signal-model of an existing T2 model-based iterative reconstruction [37] to enable the reconstruction to be applicable to a Gradient Recalled Echo (GRE) sequence in order to perform quantitative T2*-mapping, 2) studying the influence of GRE sequence parameters on the performance of the model-based reconstruction to find an ideal acquisition protocol, 3) technical realization of the algorithm in the MR scanner environment to explore its technical feasibility in a clinical setting.

## 1.2 Structure of the Thesis

This thesis is divided in six chapters and an appendix. After the introducing part in this chapter, the second chapter starts with the fundamentals of MRI, explaining the magnetic resonance phenomenon and relaxation. Furthermore, it illustrates how the basic sequences, e.g. spin echo and gradient echo, work and how they are applied to measure relaxation. Finally, the state of the art of model-based iterative reconstruction in MRI is explained. Thereby, the model is based on a real-valued signal.

The text of the third chapter lists system-related and biological effects causing the

signal to be complex-valued. The expansion of the model-based iterative reconstruction to a complex-valued signal model is demonstrated. Furthermore, different regularizations and sampling patterns are explored and their effects on the performance of the algorithm is shown. Additionally, the exploration of different sequence parameters to provide a good dataset for the reconstruction is reported. Finally, the implementation and performance optimization of a scanner implementation for T2-mapping using the real-valued signal model is explained.

Chapter four illustrates the results of applying the real-valued and complex-valued model to multi-spin echo and gradient-recalled echo datasets. Furthermore, the effect of different sequence parameters and regularizations are demonstrated. Finally, reconstruction times and outcome of the scanner implementation for T2-mapping are presented.

Chapter five discusses these results and gives an outlook on possible future extensions and improvements.

Chapter six concludes the findings of this work. Finally, the appendix contains mathematical derivations, detailed sequence protocols and the bibliography.

# 2 Theory and State of the Art

## 2.1 Fundamentals of MRI

MRI is based on the fact that water is abundant in biological tissue, thus contains protons($^1H$) having a nuclear spin. The basic motion of a proton might be understood by imagining it as an electrically charged gyroscope. It thus processes an effective loop of electric current around the same axis it is spinning. This dipole can be described as a so-called magnetization-vector.

Furthermore, the nuclear spin interacts with an external magnetic field($\vec{B_0}$) by precessing about the field direction. Thus the magnetization-vector becomes aligned with the static magnetic field. However, detecting a static magnetization-vector with a significant signal intensity is difficult. Thus, it needs to be tipped away from the external field direction, in order to set it into precession, a so-called excitation. The excitation is realized by applying a radio frequency (RF) pulse, effectively generating a varying electromagnetic field. The axis of the spin will be successfully rotated when the frequency of this pulse equals the Larmor frequency. This frequency equals the precession frequency of the atomic nuclei in the magnetic field.

After the excitation, the magnetization-vector will realign with the static magnetic field again, so-called relaxation. This motion will generate a detectable changing flux in any nearby receiver coil [17]. The different types of relaxation will be explained in the following section.

## 2.2 Relaxation

After spins have been excited, thus the magnetization vector rotated, it relaxes exponentially back into the direction of the static filed $\vec{B_0}$. The rate of this rotation depends on spin interactions and the chemical environment and can be characterized by a time-constant $T1$. This effect is called longitudinal relaxation. Figure 2.1 illustrates the exponential regrowth of the longitudinal magnetization after a 90° RF pulse.

A second relaxation effect is the transverse relaxation. This is the dephasing of spin coherences. This arises from the decorrelation of the spins within a volume. Their phases disperse due to variations in the local precession frequency. In general, signals will additional suffer from field inhomogeneities, resulting in a faster decay characterized by the time constant $T2^*$. However, this effect can be avoided by using a spin-echo sequence [17]. Figure 2.1 shows the exponential decay of the transverse magnetisation,

characterized by the time constants $T2$ and $T2^*$. Typical values for $T1$ and $T2$ at a static field strength of 1.5T and 3T are shown in Table 2.1.

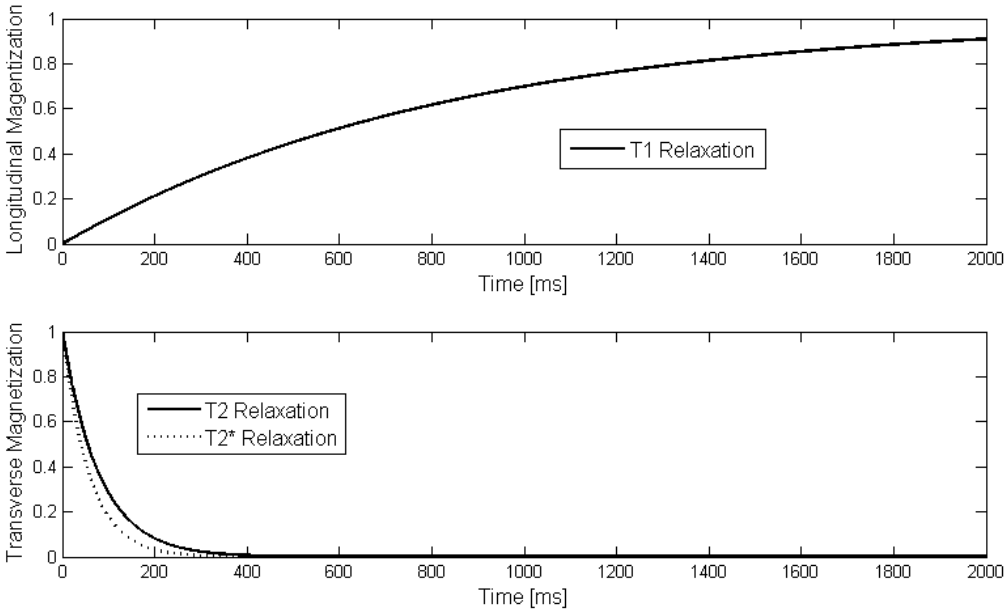


Figure 2.1: Longitudinal and transverse magnetization of simulated relaxations (T1, T2 and T2*) within a WM volume at a satic field strenth of 3T.

A property of T2 and T2* decay is, that 37% of the initial signal intensity is reached at the time point of the characterizing time constant. This has important implications if the signal is fitted to an exponential decay curve. Therefore, such a curve should be longer sampled as its characterizing time constant. However, the signal will never converge to zero due to the presence of noise. Thus, a fitting error will be introduced. Therefore, a trade-off between signal to noise ratio (SNR) and curve coverage need to be found.

| Tissue | 1.5T | | 3T | |
|---|---|---|---|---|
| | T1 [ms] | T2 [ms] | T1 [ms] | T2 [ms] |
| gray matter (GM) | 950 | 100 | 1331 | 110 |
| white matter (WM) | 600 | 80 | 832 | 79.6 |
| cerebrospinal fluid (CSF) | 4500 | 2200 | - | - |

Table 2.1: Values of relaxation parameters T1 and T2 for hydrogen components of different human brain tissue at a static field strength of 1.5T and 3T. These are only approximate values [17, 41].

## 2.3 K-Space

The signal acquired in MRI is measured in the frequency domain using RF pulses and magnetic gradient fields. For convenience, the frequency domain is defined in MRI with respect to the applied gradient fields:

$$K(t) = \gamma \int_0^t G(t)dt \tag{2.1}$$

where $G$ is the gradient field amplitude over time and $\gamma$ the gyromagnetic ratio [17].

The k-space is hence a matrix of complex numbers containing magnitude and phase frequency information. These frequencies represent an object in image space. The low frequencies are in the k-space center and describe the main anatomical information and image contrast. High frequencies are at the outer k-space regions and represent the image resolution, thus the edges of the image. The measured image can be reconstructed by performing an inverse Fourier transform (iFT) on the fully sampled k-space. Figure 2.2 illustrates an exemplary MR-image obtained by the iFT of the k-space magnitude and phase.

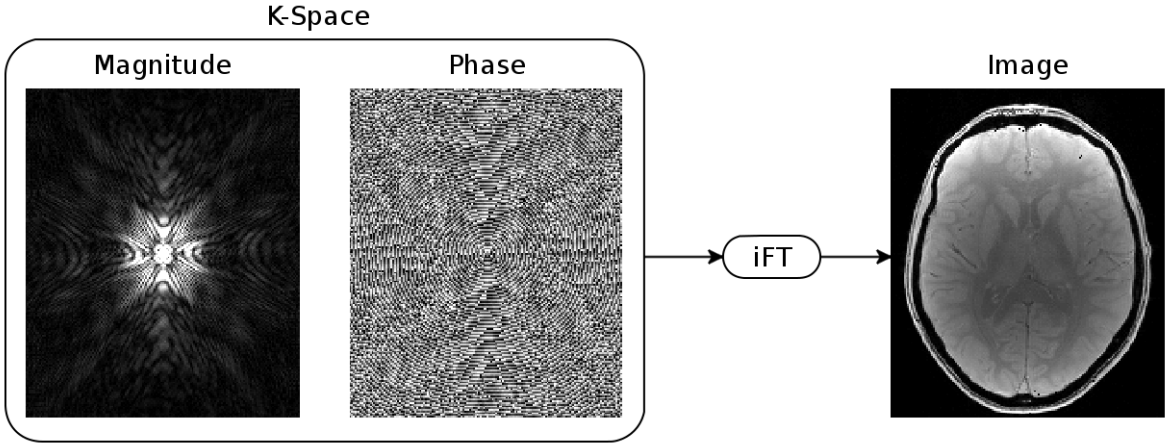


Figure 2.2: Examplary image reconstruction by performing an inverse Fourier transform(iFT) on the k-space.

In the following a simple gradient or spin-echo acquisition scheme is assumed for clarity. The k-space is filled line-wise during a MR measurement. Thereby the sampling along one line is called read-out and is performed within milliseconds using an analogue-digital converter (ADC) and a simultaneously applied linear gradient. The position of this line in k-space can be manipulated by applying a phase encoding gradient directly after the excitation, its strength influences the distance of the phase encoding step. One line is measured per repetition time (TR), because the target volume needs to be excited for each phase-encoding step. Figure 2.3 illustrates the above explained line-wise k-space filling.

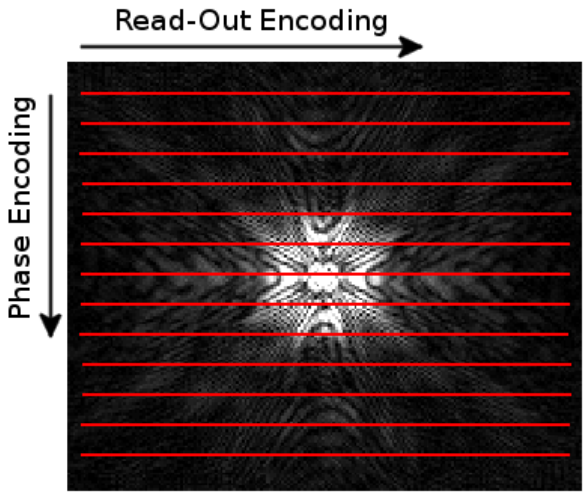


Figure 2.3: Line-wise filling of the k-space with several phase-encoding steps.

## 2.4 Imaging Sequence

In a basic MRI protocol, a single echo is acquired and reconstructed with an inverse Fourier transform. In doing so, the sampled echo is stimulated to occur at a specific delay after the excitation, the echo time (TE). Thereby, TE defines the contrast between the tissues as consequence of varying spin relaxation. However, to reconstruct quantitative maps, the evolution of the signal over time needs to be measured. Thus, several images with different TE's, hence different contrast have to be measured. This is done by using so-called multi echo acquisitions. The images with different contrast can than be reconstructed by performing an inverse Fourier transform for each TE.

In this project, a Multi-Spin Echo (MSE) sequence is used to sample the transverse relaxation driven by T2 and a GRE is used to sample relaxation driven by T2*. These two sequences will be explained in the following sections.

### 2.4.1 Spin-Echo-Sequence

In a spin-echo experiment, the spins are first excited with a 90° RF pulse. Afterwards, the spins precess at slight different velocities proportional to their local magnetic field strength and dephase. Consequently, a 180° RF pulse is applied, flipping the spins 180° on the transverse plane. This pulse does not effect the precession frequencies of the spins but inverts their phase angles. Thus, the spins will rephase and come back along one vector, forming the spin echo, after a time equal to the delay between the 90° and 180° RF pulse. This phase-reversal will cancel out the influence of field inhomogeneities and tissue susceptibility differences. Consequently, the echo amplitude only depends on T2. The 180° pulse can be applied repeatedly to stimulate multiple echoes with amplitudes according to the T2-decay[25].

Figure 2.4 illustrates a sequence diagram of a simple MSE sequence. Thereby, $G_{ss}$ denotes the slice selection, $G_{pe}$ phase-encoding and $G_{ro}$ the read-out gradient. The slice-selection gradient is applied simultaneously to the RF pulse. This gradient adds a linear magnetic field on the main static field, thus the spins precess with a spatially dependent frequency. Hence, a bandwidth limited RF pulse excites only a selective sub-volume. Furthermore, the phase encoding gradient is applied in order to select which line in k-space is measured. Thereby, the larger the area under the gradient, the further is the phase-encoding step $\triangle k_y$ away from the k-space center. Finally, the read-out encoding gradient is applied simultaneously to the sampling, also called frequency encoding.

The precision of these gradients is very important to perform an accurate measure, especially how strong and how long they are applied. Thus the areas under curve ($A_{ss}$,$A_{ro}$) should be well maintained to produce good image quality.

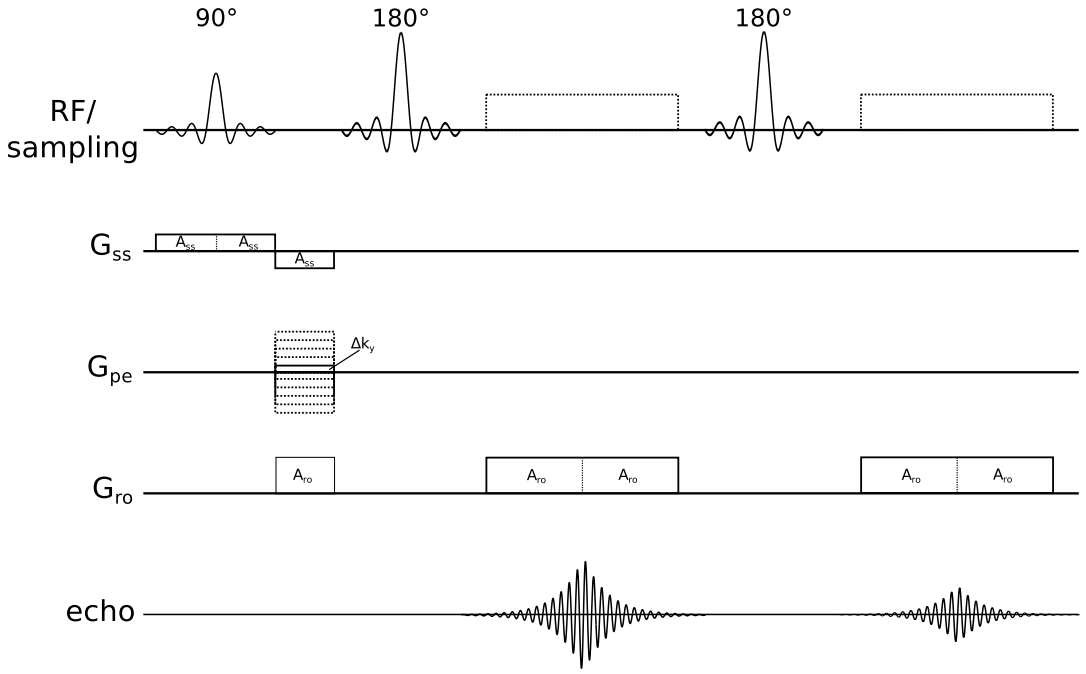


Figure 2.4: Sequence diagram of a multi-spin-echo sequence, producing two echoes by apllying two 180° RF-pulses.

### 2.4.2 Gradient-Echo-Sequence

The main difference of a gradient-recalled-echo experiment compared to a spin-echo experiment is that the echo is formed using gradient fields.

In doing so, the spins are first excited with a RF-pulse. Thereby, the flip-angle of the RF-pulse is typically lower than 90° (e.g. 20°). Afterwards, a negative gradient lobe is applied causing the spins to dephase much faster than normally. Then, a positive lobe is

applied which simply reverses the magnetic field gradient. Spins that were precessing at a low frequency due to their position in the gradient will now precess at a higher frequency because the gradient will now add to the main field, and vice versa. Therefore the spins start to rephase and form the gradient echo along a vector. However, the positive gradient only compensates for the dephasing caused by the negative gradient lobe, not for field inhomogeneities or spin-spin relaxation. Consequently, the echo amplitude depends on T2* [25]. The spins will start to dephase again, when the positive gradient is kept applied after the first echo. Afterwards, a negative gradient is applied to force the spins to rephase again, forming another echo. This process can be repeated to generate multiple echoes. Thereby, the echoes are caused by gradients with different polarity, therefore is called bi-polar GRE. Figure 2.4 shows a sequence diagram of a simple bi-polar GRE sequence.

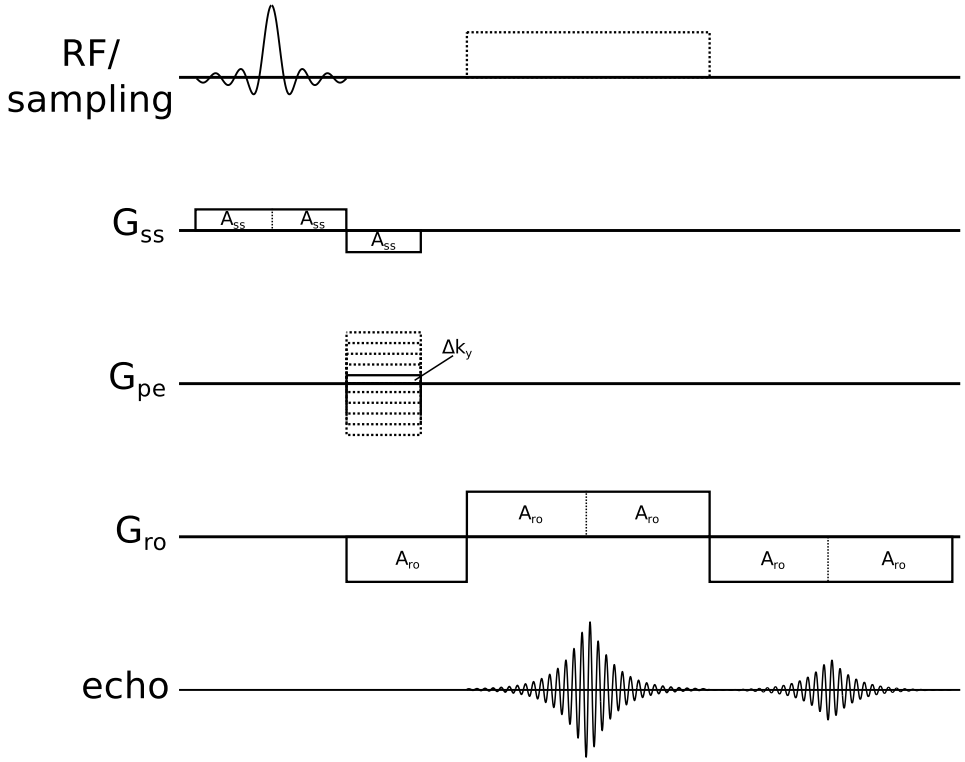


Figure 2.5: Sequence diagram of a bi-polar gradient recalled echo sequence, producing two echos by applying positive and negative gradient lobes during sampling.

However, acquiring echoes caused by gradients with different polarities can be disadvantageous due to system related effects and imperfections. Another option is to apply a strong negative gradient after the positive gradient, causing the spins to rephase and dephase rapidly without sampling. Afterwards, the rephasing with a positive polarity is measured again. Therefore, all echoes are acquired with gradients of the same polarity. This technique is known as mono-polar or uni-polar GRE. The corresponding sequence

diagram is shown in Figure 2.5.

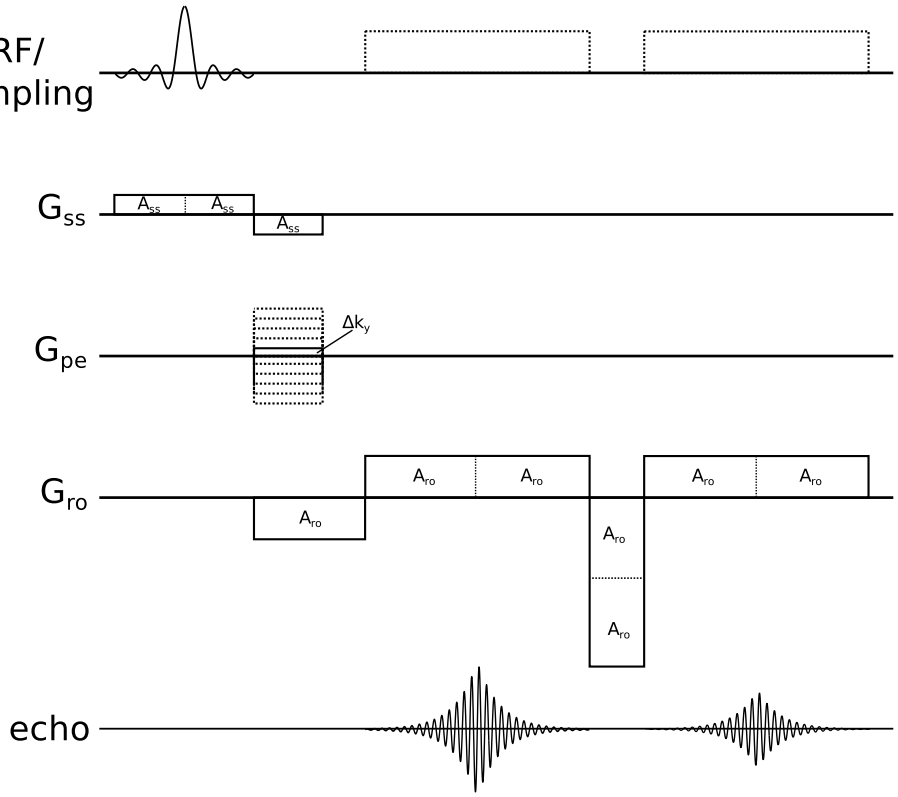


Figure 2.6: Sequence diagram of a mono-polar gradient recalled echo sequence, producing two echos by applying only positive gradient lobes during sampling.

### Flow Compensation

In MRI artifacts caused by flow (e.g. blood flow) can degrade the image quality. These artifacts arise from phase dispersion across a voxel due to motion. Therefore, a method has been developed to compensate for flow with constant velocity. This flow compensation applies a further gradient lobe to ensure that the phase at the echo is zero for both stationary and constant velocity moving spins [17]. However, this additional gradient increases acquisition time. Thus, the benefit of compensating flow for a specific application such as the model-based iterative reconstruction needs to be weighted up with the additional acquisition time.

## 2.5 Model-Based Iterative Reconstruction

Sumpf et al. suggested an iterative non-linear Reconstruction in order to reconstruct T2-maps [37]. The present work is based on this algorithm, which assumes the measured

signal to be real-valued. The theory of this algorithm will be explained in the following sections.

### 2.5.1 Model Definition

In a MR-experiment, the signal is measured in the frequency domain. Therefore, the retrieved signal of a single coil can be mathematical described as follows,

$$s(u) = \int M(\vec{r}) e^{-i\vec{r}\vec{k}(u)} d\vec{r}. \tag{2.2}$$

This is the Fourier transform of the magnetization $M$ in the image domain. The vector $\vec{r}$ denotes the position in image-space and $\vec{k}(u)$ the $u$th sample point on the k-space trajectory. The trajectory describes the sampling scheme, such as radial, spiral or Cartesian sampling. To simplify the notation, the Fourier transform will be further denoted as operator $\mathcal{F}$ and the inverse Fourier transform as $\mathcal{F}^{-1}$

The exponential decay over time $t$ of the magnetization is the prior-knowledge of the model. Figure 2.7 shows an exemplary magnetization, measured with a MSE sequence within a white-matter voxel. The mathematical description of the measured magnetization at echo time $t$ can be formulated as follows,

$$M_t(\vec{r}, \rho, R) = \rho(\vec{r}) e^{-R(\vec{r})t}. \tag{2.3}$$

The magnitude of the magnetization depends on the proton density $\rho$, specifying the signal intensity at echo time zero and the exponential decay due to the relaxation rate $R$. The tissue specific relaxation time constant can be calculated by $T = \frac{1}{R}$.

Hence, the in k-space expected signal at echo-time $t$ of a parameter map estimate can be modelled by inserting equation (2.3) in equation (2.2):

$$x_t(\rho, R) = \mathcal{F}(\rho(\vec{r}) e^{-R(\vec{r})t}). \tag{2.4}$$

This prior-knowledge of the signal-modulation can be used to design a cost-function, in order to validate the quality of a parameter estimate and update this estimate iteratively, using an optimizer. The goal is to apply this parameter estimate on under-sampled data to recover missing sample-points.

### 2.5.2 Iterative Optimization Process

To start an iterative reconstruction, the optimizer has to be initialized with an initial guess of the relaxation map $R$ and proton density map $\rho$. This guess could be a homogeneous map of expected average values. The goal of the iterative reconstruction is to evaluate the quality of this estimate with a cost function and minimize the cost by changing the estimate using an optimizer.

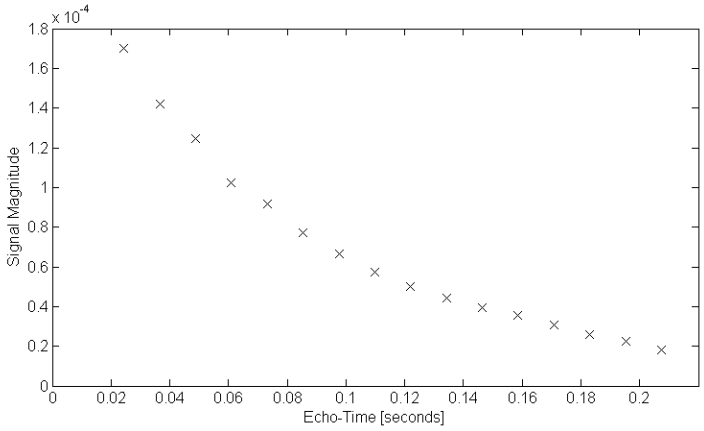


Figure 2.7: Measured exponential decay of the magentization in a multi spin echo experiment. The plot displays a typical in-vivo decay in white-matter. The slope of the decay can be parameterized by the time constant T2. The signal magnitude at echo-time zero is the proton-density $\rho$.

Thereby, the estimation takes place in the image domain, but the quality of this estimate is evaluated in the data-format of the measured signal, consequently in k-space. Thus, the estimated maps need to be transformed into the same data format as the measured data, in order to be comparable. The data format of the measurement is the under-sampled k-space for each echo time. Hence, applying the model (exponential decay), considering the proton-density and relaxation time of the current estimate, yield magnitude images for each echo. The data is comparable after applying a Fourier transform and artificial down-sampling, by multiplying with a binary mask. The comparison is done by calculating the residuum between estimate and measured data and taking the $l2$-norm, yielding the cost function value $\phi$. Thereby $\phi$ can be described as a mathematical function of the relaxation-rate $R$ and proton-density $\rho$. In this project a conjugate gradient descend (CG-descend) algorithm is used in a black box manner to minimize the cost-function-value $\phi$. The CG-descend algorithm was originally proposed by Hager and Zhang[18] and is available as a C-implementation. This algorithm is performing a line search along the gradients of the estimate maps, in order to get closer to the solution. Thus, the derivatives of the cost-function with respect to each parameter needs to be provided to the optimizer. After this line-search along the gradients, a new estimate has been calculated and needs to be evaluated. Therefore the process is restarted iteratively, till a stop criterion has been reached. The standard stop criteria are, reaching a tolerable cost-function-value (ideally zero) or reaching the maximum number of iterations. Then, the current estimate is considered as the final result which consist of relaxation and proton-density maps. Figure 2.8 illustrates the process of the above explained algorithm.

To sum up, the most important steps are providing a cost-function and the gradients of this cost-function to the optimizer.

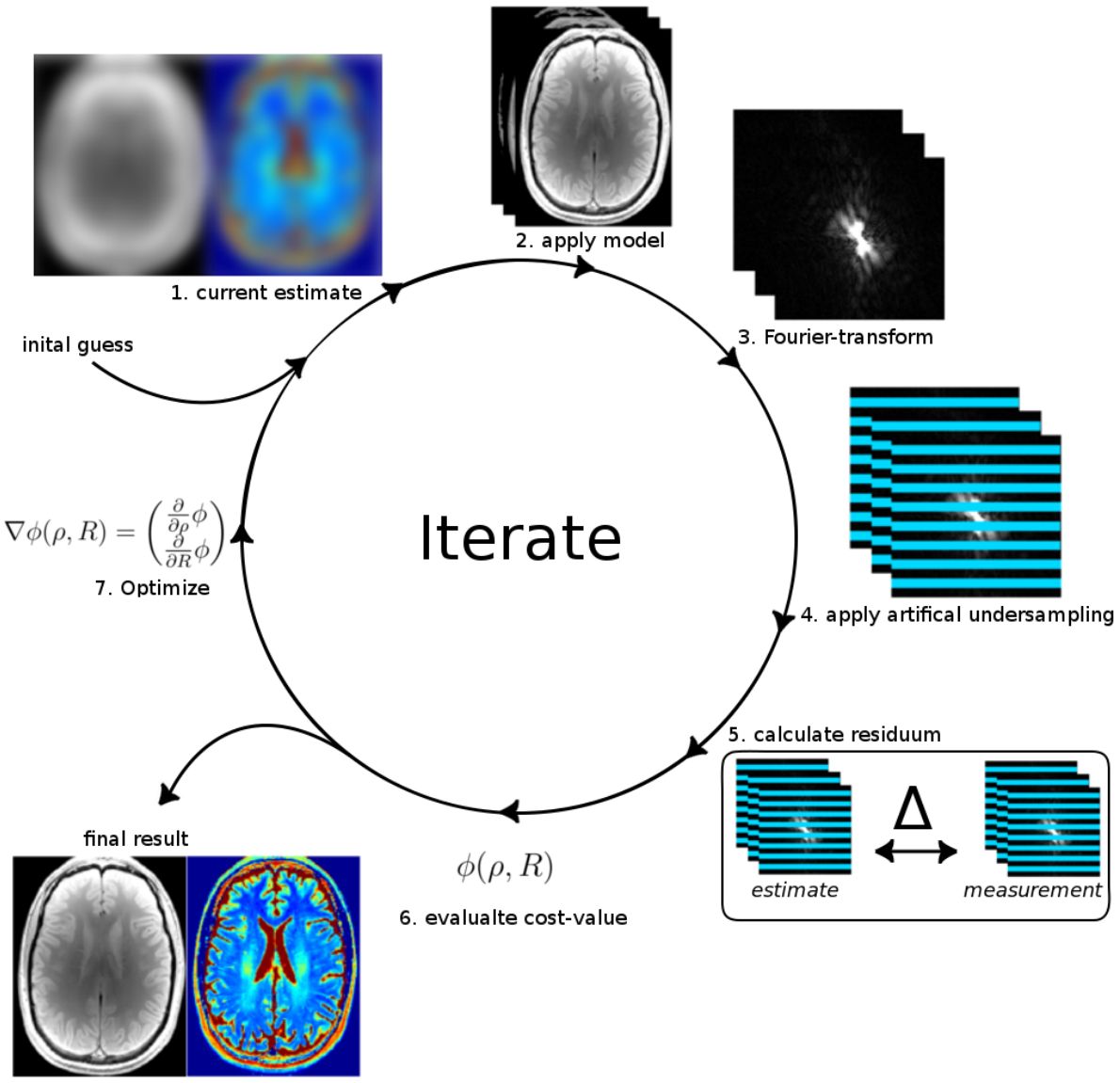


Figure 2.8: Illustration of the iterative reconstruction and its single steps explained in section 2.5.2

### 2.5.3 Cost Function

As explained in the previous section, the optimizer needs a cost function $\phi$ that evaluates the quality of the current estimate of relaxation-ratio $R$ and proton-density $\rho$. The goal is to minimize this function with respect to $R$ and $\rho$.

$$\underset{R,\rho}{\operatorname{argmin}}\, \phi(R, \rho) \tag{2.5}$$

The cost of the current estimate can be calculated by taking the $l2$-norm of the residuum between estimate and measured data. For this reason the estimate needs

to be transformed into the same data format as the measurement by using the prior-knowledge of the signal model, described by eq. (2.4), and an artificial down-sampling. This can be mathematically described as followed,

$$\phi(\rho, R) = \frac{1}{2} \sum_{t} \|P x_t(\rho, R) - y_t\|_2^2 \tag{2.6}$$

where $y_t$ denotes the measured under-sampled k-space at echo time $t$ and $P$ a binary mask to apply artificial down-sampling to the k-space of the estimate $x_t$.

### 2.5.4 Multiple Receiver Coils

The usage of multiple receiver coils have become essential for parallel imaging techniques [33, 35, 16]. It has been proven that the image quality highly depends on the number and arrangement of the coil-elements [42, 31]. Furthermore, increasing the number of coil-elements enhances the object coverage, thus simplifying the set-up and patient preparation process. Due to this developments, the number of used coil-elements increased from typical six/eight to 32 and more, recently in clinical practice [4].

Therefore, cost-function (2.6) would not be applicable in clinical practice. Consequently, not a single signal but multiple signals with varying spatial coverage are measured simultaneously.

Recently, several algorithms have been developed to determine the spatial coverage of a single coil-element within a coil-array [33, 22, 38]. These algorithms use a small amount of data to estimate coil-sensitivity maps for each coil element. Examples of the resulting coil sensitivity maps are shown in Figure 2.9.

These coil sensitivity maps can be used to model the usage of multiple receiver coils. In doing so, the estimate is weighted with the sensitivity maps, yielding multiple images with different object coverage. This weighting factor $C_c$ will change the cost-function (2.6) as follows,

$$\phi(\rho, R) = \frac{1}{2} \sum_{c} \sum_{t} \|P x_t(\rho, R) C_c - y_{c,t}\|_2^2. \tag{2.7}$$

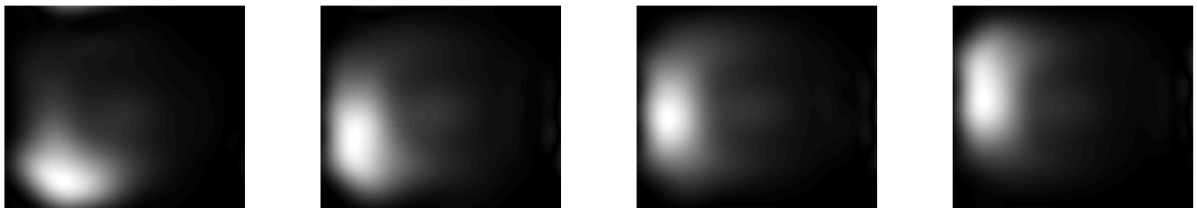

Figure 2.9: Coil sensitivities of four coil elements out of a 32 head coil array, estimated with the algorithm proposed by Uecker et al. [38].

### 2.5.5 Simplification and Problem-Scaling

For performance reasons, the cost function can be modified to reduce the computational time. Even minor changes have an essential impact to the performance, due to the high number of iterations.

First, the term $e^{-Rt}$ can be reformulated to $(e^{-R\triangle t})^n$, yielding a constant value $\hat{R} = e^{-R\triangle t}$, where $n$ is the index of the echo. This assumes that the echo-spacing $\triangle t$ is equal for all echoes. Using this simplification the magnetization-model (2.3) changes to,

$$M_n(\rho, \hat{R}) = \rho \hat{R}^n. \tag{2.8}$$

where the position vector $\vec{r}$ is neglected to simplify notation.

Second, a gradient scaling suggested by Block et al.[3] improves the convergence rate of the optimizer dramaticly. The gradient scaling is resolving the common problem of widely differing magnitudes. This can be due to differing physical units of the parameters. For example, one parameter could be given in kilometres ($10^3$ metres) and a second one in milliseconds($10^{-3}$ seconds) leading to significant differences in the magnitude of the gradients [26]. In order to resolve that problem, scaling-factors for each parameter have to be added into the magnetization model (2.8):

$$M_n(\tilde{\rho}, \tilde{R}) = L_\rho \tilde{\rho} L_R \tilde{R}^n. \tag{2.9}$$

The tilde denotes a scaled parameter, such that $\rho = L_\rho \tilde{\rho}$ and $\hat{R} = L_R \tilde{R}$.

The value of a parameter-scaling-factor is calculated by deriving equation (2.9) with respect to the parameter, norm it to one and transpose it to its scaling factor, yielding the following equations

$$\begin{aligned} L_\rho &= \frac{1}{\sum_n R^n} \\ L_R &= \frac{1}{\sum_n \rho n R^{n-1}} \end{aligned} \tag{2.10}$$

Inserting mean values of the initial guess into equation (2.10) proofed to yield balanced gradient magnitudes and consequently a better convergence rate [37]. Figure 2.10 illustrates this effect by showing an unscaled and scaled solution space of a single voxel. After performing a two step line search, the optimizer is much closer to the solution in a scaled as in an unscaled solution-space.

This simplification and gradient-scaling will change the cost function as follows

$$\phi(\tilde{\rho}, \tilde{R}) = \frac{1}{2} \sum_c \sum_n \| P\mathcal{F}(M_n(\tilde{\rho}, \tilde{R}) C_c) - y_{c,n} \|_2^2. \tag{2.11}$$

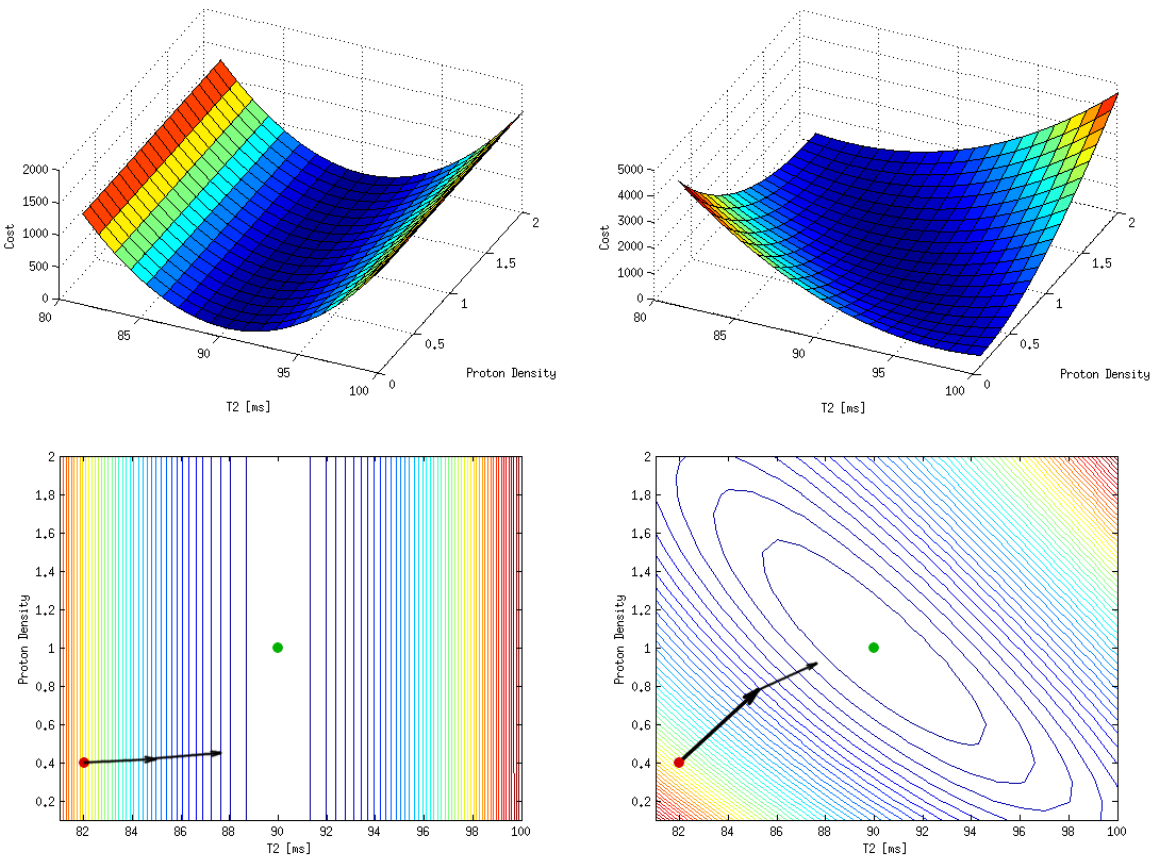


Figure 2.10: The first row shows the surface plots of an unscaled(left) and scaled(right) solution space for an exponential decay. The second row shows the course of a line search within the solution spaces, starting with the same initial guess(red dot). After two steps, the optimizer of the scaled solution space is much closer to the solution (green dot) than the unscaled solution space.

### 2.5.6 Gradient Calculation

The gradients needed by the optimizer are calculated by deriving the cost function with respect to its parameters $\rho$ and $R$.

$$\nabla\phi(\rho, R) = \begin{pmatrix} \frac{\partial}{\partial\rho}\phi \\ \frac{\partial}{\partial R}\phi \end{pmatrix} \tag{2.12}$$

First, the simplified cost function,

$$\phi(p) = \frac{1}{2}\|X(p) - Y\|_2^2. \tag{2.13}$$

can be partially derived with respect to an parameter $p$ with the following rule

$$\frac{\partial}{\partial p}\phi(p) = \Re\{(X(p) - Y)\frac{\partial}{\partial p}\overline{X(p)}\}. \tag{2.14}$$

where $\overline{X}$ denotes the complex conjugate of $X$. The mathematical derivation of this formula is given in the Appendix 7.1.1 [3].

The gradient of the cost function (2.11) can now be calculated as follows,

$$\begin{aligned}\frac{\partial}{\partial \tilde{\rho}}\phi &= \sum_c \sum_n L_\rho \hat{R}^n \Re\{\overline{C_c}\mathcal{F}^{-1}(P\mathcal{F}(M_n(\rho, \hat{R})C_c) - y_{c,n})\} \\ \frac{\partial}{\partial \tilde{R}}\phi &= \sum_c \sum_n L_R \rho n \tilde{R}^{n-1} \Re\{\overline{C_c}\mathcal{F}^{-1}(P\mathcal{F}(M_n(\rho, \hat{R})C_c) - y_{c,n})\}\end{aligned} \tag{2.15}$$

# 3 Methods and Materials

## 3.1 Expansion of Model to Complex Signals

The above explained algorithm has been proven to work robustly on multi-spin-echo data, to map the transverse relaxation T2 [37]. However, applying it on a dataset acquired with a GRE sequence to map the T2* relaxation fails. This is due to system-related and biological effects, causing the signal to be complex-valued. Thus, the signal needs to be expanded to fit the data in magnitude and in phase domain. These effects and expansion of the model will be explained in the following sections.

### 3.1.1 System-Related and Biological Effects

Several system related and biological effects in a gradient echo sequence can cause the signal to be complex valued.

For example, a biological effect is the tissue specific magnetic susceptibility. This effect is an important source of contrast in MRI. As in case of fMRI, the change in local susceptibility is measured in order to indicate an activated brain region. Thereby, the magnetic susceptibility in blood vessels varies due to changes in the oxygen concentration, the blood oxygen level dependent (BOLD) effect[24].

Furthermore, the signal can be corrupted by non-tissue specific effects. For example, using a bi-polar GRE sequence can cause inconsistencies between odd and even echoes, in literature known as odd-even-effect. Errors occurring in the phase domain are mainly induced by gradient imperfections and eddy currents. The strongest effect is a shift of the echo-peak along the read out direction in k-space. This induces a linear phase error in the image-domain along the same direction. Remaining phase errors in all directions could be caused by eddy currents and other conducting structures in the system, such as radio-frequency shield, concomitant gradients and cross term eddy currents.

Furthermore, errors also can be induced into the magnitude domain, caused by receiver chain filters, visible as an asymmetric magnitude modulation depending on the gradient polarity[48].

Modelling these effects for the iterative reconstruction could be one way to deal with the artifacts. However, this would increase the model complexity dramaticly, by increasing the number of parameters, hence reducing the robustness of the algorithm. In this project, a mono-polar GRE sequence has been used to reduce the effect of these errors. Actually, the above explained errors are present in every echo of the mono-polar GRE as

well. Effectively, these phase errors are added constantly on each echo, thus the relative phase between the echoes remain unchanged.[48]

Another source of errors are susceptibility effects caused by field inhomogeneities. These inhomogeneities may arise from placing an object in the magnetic field. The main inhomogeneities can be suppressed by applying an antagonize magnetic field, so-called shimming. However, shimming cannot suppress small variations, especially at the location of air-tissue interfaces. For example around the nasal cavity, inferior frontal and lateral temporal lobes. These inhomogeneities induce a magnetic field gradient within a voxel, causing spins to dephase and mutually cancel. Thus, the magnetization appears to decay with a shorter $T2^*$. Therefore, the estimated relaxation-map contains areas with underestimated $T2^*$ values [5]. In the past, several solutions to reduce susceptibility effects have been proposed. For example, using adjustable slice selection gradients proposed by Frahm et al. [11] or tailored radio-frequency pulses proposed by Cho et al. [5]. Furthermore several methods to correct susceptibility effects a posteriori have been proposed, such as gradient-echo-slice-excitation-profile-imaging (GESEPI) [46], voxel-spread-functions [45] and sinc-approximations [9]. In this project, the reduction of susceptibility artifacts is accomplished by decreasing the voxel size, hence decreasing the magnetic field difference within a voxel. However, this method is restricted by the SNR [47]. The remaining phase errors can be described as a linear function, thus can be modelled with two parameters and added into the iterative reconstruction. How to adapt the model in order to introduce these two parameters will be explained in the following sections.

### 3.1.2 Adapted Signal Model

Figure 3.1 is showing a typically measured dataset for a mono-polar GRE sequence. The magnitude of the magnetisation $M_\sigma$ can be identically mathematically described as in Section 2.5.1,

$$M_{\sigma,t}(\rho, R) = \rho e^{-Rt} \tag{3.1}$$

Additionally, the phase can be described by a linear function

$$M_{\theta,t}(b, \varphi_0) = 2\pi bt + \varphi_0 \tag{3.2}$$

where $b$ denotes the frequency shift over time in Hz. This frequency shift is caused by field inhomogeneities and reflects the slope of the phase error. Estimating this value with respect to a location $\vec{r}$ is called field-mapping. The variable $\varphi_0$ denotes the phase at echo time zero. This effect may be induced by transmit and receive RF field inhomogeneities.

Finally, a Fourier transform has to be applied to model the expected signal for the current estimate in k-space.

$$x_t(\rho, R, b, \varphi_0) = \mathcal{F}(M_{\sigma,t}(\rho, R)e^{iM_{\theta,t}(b,\varphi_0)}) \tag{3.3}$$

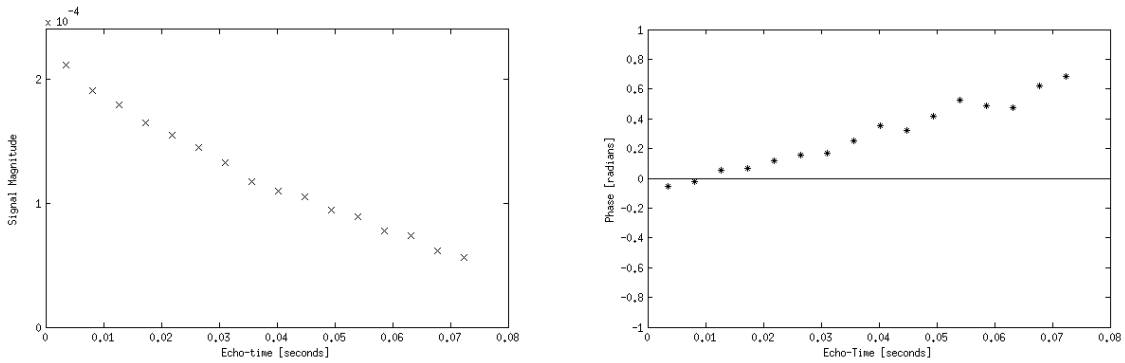


Figure 3.1: Magnitude(left) and phase(right) of a white-matter voxel measured in-vivo with a monopolar gradient echo sequence.

### 3.1.3 Adapted Cost- and Gradient Functions

A gradient scaling needs to be applied to this signal according to Section 2.5.5. By doing so a scaling factor needs to be added for each parameter as follows

$$\begin{aligned} M_{\sigma,t}(\tilde{\rho}, \tilde{R}) &= L_\rho \tilde{\rho} e^{-L_R \tilde{R} t} \\ M_{\theta,t}(\tilde{b}, \tilde{\varphi_0}) &= 2\pi L_b \tilde{b} t + L_{\varphi_0} \tilde{\varphi_0} \end{aligned} \tag{3.4}$$

The correct scaling factors should accomplish a balanced magnitude of gradients by norming them to one. Those factors can be archived with the following equations,

$$\begin{aligned} L_\rho &= \frac{1}{\| \frac{\partial}{\partial \tilde{\rho}} \phi \|_2} \\ L_R &= \frac{1}{\| \frac{\partial}{\partial \tilde{R}} \phi \|_2} \\ L_b &= \frac{1}{\| \frac{\partial}{\partial \tilde{b}} \phi \|_2} \\ L_{\varphi_0} &= \frac{1}{\| \frac{\partial}{\partial \tilde{\varphi_0}} \phi \|_2} \end{aligned} \tag{3.5}$$

Effectively, each scaling factor can be calculated by inverting the norm of the deviation of the cost function, where the deviations are shown in equation (3.9).

Finally, the cost function considering a complex magnetization, gradient scaling and multiple receiver coils can be formulated as follows

$$\phi(\tilde{\rho}, \tilde{R}, \tilde{b}, \tilde{\varphi_0}) = \frac{1}{2} \sum_c \sum_t \| P x_t(\tilde{\rho}, \tilde{R}, \tilde{b}, \tilde{\varphi_0}) C_c - y_{c,t} \|_2^2 \tag{3.6}$$

with

$$x_t(\tilde{\rho}, \tilde{R}, \tilde{b}, \tilde{\varphi_0}) = \mathcal{F}(M_{\sigma,t}(\tilde{\rho}, \tilde{R}) e^{iM_{\theta,t}(\tilde{b}, \tilde{\varphi_0})}) \tag{3.7}$$

The cost function has now four parameters due to the expansion of the signal model, thus the gradient vectors for the optimizer have four directions. Each direction equals the deviation of the cost function with respect to one parameter.

$$\nabla\phi(\tilde{\rho}, \tilde{R}, \tilde{b}, \tilde{\varphi_0}) = \begin{pmatrix} \frac{\partial}{\partial\tilde{\rho}}\phi \\ \frac{\partial}{\partial\tilde{R}}\phi \\ \frac{\partial}{\partial\tilde{b}}\phi \\ \frac{\partial}{\partial\tilde{\varphi_0}}\phi \end{pmatrix} \tag{3.8}$$

Equivalent to the previous model, the derivatives can be calculated by using rule (2.14),resulting the following equations:

$$\begin{aligned} \frac{\partial}{\partial\tilde{\rho}}\phi &= \sum_c \sum_t L_\rho e^{-Rt} \Re\{K_{c,t}\} \\ \frac{\partial}{\partial\tilde{R}}\phi &= \sum_c \sum_t -L_R \rho t e^{-Rt} \Re\{K_{c,t}\} \\ \frac{\partial}{\partial\tilde{b}}\phi &= \sum_c \sum_t L_b \rho e^{-Rt} \Re\{-i2\pi t K_{c,t}\} \\ \frac{\partial}{\partial\tilde{\varphi_0}}\phi &= \sum_c \sum_t L_{\varphi_0} \rho e^{-Rt} \Re\{-i K_{c,t}\} \\ K_{c,t} &= e^{-i(2\pi bt + \varphi_0)} \overline{C_c} \mathcal{F}^{-1}(P x_t(\rho, R, b, \varphi_0) C_c - y_{c,t}) \end{aligned} \tag{3.9}$$

The mathematical derivation of these formulas are given in the Appendix 7.1.2.

### 3.1.4 Implementation

The above explained algorithm has been implemented in MATLAB. The result is a framework for model-based iterative reconstruction, where the cost function and gradient function can be easily changed and tested on phantom and in-vivo datasets. This framework also includes tools and components, such as a tool to extract MATLAB compatible data-formats from binary raw data of the scanner. Furthermore, components to evaluate the quality of the outcome. Therefore, an implementation of the quantitative mapping standard approach on fully sampled data has been realized. In particular, a pixel by pixel mono-exponential fit for proton-density $\rho$ and T2* and several methods to estimate the field map $b$ and initial phase $\varphi_0$ (e.g. linear regression[44], spatial unwrapping[15]) have been implemented.

## 3.2 Regularization

Regularization is a further approach of inserting more prior-knowledge into the signal model. The application of regularizations penalizes non-expected behaviour of the signal with respect to an assumption. For example, such an assumption could be expecting a signal to be smooth or always positive.

To apply a regularization, the penalty is added onto the cost function and its influence is weighted with a factor $\lambda$. The application of an arbitrary regularization $R_i$ on a simplified cost function is shown in the following equation:

$$\phi = \frac{1}{2}\|X - Y\|_2^2 + \lambda R_i(x) \tag{3.10}$$

Consequently, the cost of the estimate increase when the assumption of the regularization is not satisfied. Thus, the regularization functions need to be deviated to calculate the gradients of the cost function, when using a gradient-decent optimizer.

One simple regularization is penalizing un-realistic values such as a negative proton-density or a negative relaxation time. This is done by simply penalizing the cost function with the square of every negative value in the corresponding parameter-map [1]:

$$\begin{aligned} R_{pos}(g) &= \sum_j \psi(g(r_j)) \\ \psi(v) &= \begin{cases} v^2 & \text{if} \quad v < 0 \\ 0 & \text{if} \quad v \geq 0 \end{cases} \end{aligned} \tag{3.11}$$

Thereby $g(r_j)$ denotes the pixel value of an arbitrary image $g$ at position $r_j$.

Another established method is the total variation (TV) regularization, original proposed by Rudin et al. for de-noising [34]. Using this approach will assume that the object in the image consist of areas with constant intensity. The corresponding penalty is calculated by the summation of the $l1$-norm of the finite difference.

$$R_{TV}(g) = |D_x(g)| + |D_y(g)| \tag{3.12}$$

where the finite difference in x-direction $D_x$ and in y-direction $D_y$ is defined as follows:

$$\begin{aligned} D_x(g) &= g(x-1, y) - g(x, y) \\ D_y(g) &= g(x, y-1) - g(x, y) \end{aligned} \tag{3.13}$$

An expansion of TV-regularization is the total variation of the second order (TV2) [14]. It assumes that the object in the image consist of areas with gradients. Similar to the TV, the penalty is calculated by the summation of the $l1$-norm of the finite difference, but second order:

$$R_{TV2}(g) = |D_x^{(2)}(g)| + |D_y^{(2)}(g)| + |D_{xy}^{(2)}(g)| + |D_{yx}^{(2)}(g)| \tag{3.14}$$

where the finite difference of second order in x-direction $D_x$, y-direction $D_y$ and diagonals $D_{xy}$, $D_{yx}$ is defined as follows

$$\begin{aligned} D_x^{(2)}(g) &= g(x-1,y) - 2g(x,y) + g(x+1,y) \\ D_y^{(2)}(g) &= g(x,y-1) - 2g(x,y) + g(x,y+1) \\ D_{xy}^{(2)}(g) &= g(x+1,y+1) - 2g(g,y) + g(x-1,y-1) \\ D_{yx}^{(2)}(g) &= g(x+1,y-1) - 2g(g,y) + g(x-1,y+1). \end{aligned} \tag{3.15}$$

Knoll et al. proposed a combination of TV and TV2 [20]. This combination is known in literature as total generalized variation (TGV). It has been proven to fit the signal of a structured MR brain image well, by allowing both constant areas and gradients in the image object. The TGV regularization has shown to be very effective to remove truncation artifacts [2] and is defined as follows

$$R_{TGV}(g) = \gamma R_{TV}(g) + (1-\gamma) R_{TV2}(g) \tag{3.16}$$

where $\gamma$ is a weighting factor in order to balance between TV and TV2. In this work $\gamma = 0.77$ will be used as suggested by Geman et al. [14].

A quadratic regularization is a good choice to penalize non-smooth signals. This regularization is well established for coil sensitivity estimations [38] and field map estimations [32, 13]. Funai et al. suggest a quadratic regularization for field map estimations by using the finite difference of the second order to penalizing the cost function with the following equation:

$$R_{field} = \frac{D_x^{(2)}(g)^2}{2} + \frac{D_y^{(2)}(g)^2}{2} + \frac{D_{xy}^{(2)}(g)^2}{2} + \frac{D_{yx}^{(2)}(g)^2}{2} \tag{3.17}$$

The above explained regularizations have been implemented in this project. Thereby the performance of each regularization has been tested on numerical phantoms. Figure 3.2 shows the different effect of TV, TV2, TGV and a quadratic regularization on these phantoms corrupted with Gaussian noise. Finally, the regularizations have been integrated into the framework of the model-based iterative reconstructions and can be easily applied. Thereby, the weighting values $\lambda$ have been evaluated in a brute force approach by first, reconstructing with small weighting-values and second, increasing the influence till the desired regularization level is reached.

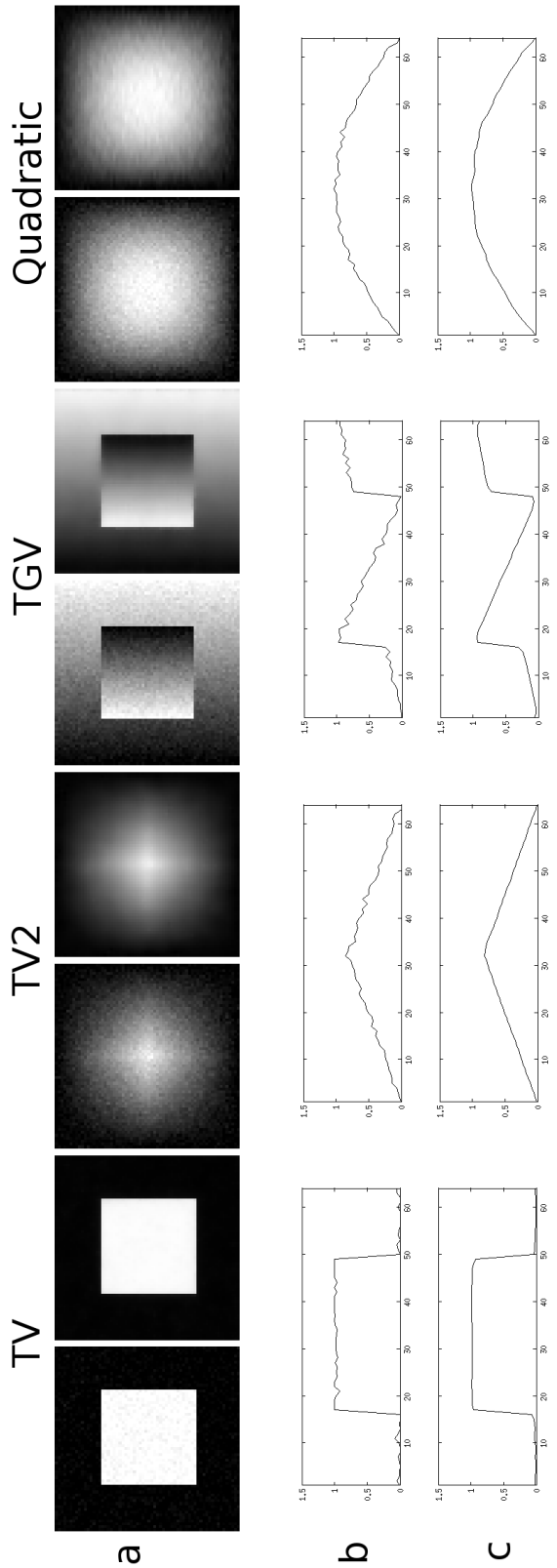


Figure 3.2: Overview of different regularizations on phantoms corrupted with Gaussian noise. In row a) are several phantoms, one corrupted with gaussian noise (left) and the result after regularization with a signal corresponding method(right) for each regularization. Row b) shows the profile of a line within the noise corrupted phantom and row c) the profile of a line in the regularized phantom.

## 3.3 Sampling Patterns

Theoretically, the model based reconstruction is independent to the used under-sampling pattern as long the signal corresponds ideally to the model. However, in-vivo measurements never correspond ideally due to the present of effects, such as noise, motion artifacts and blood-flow. Thus the sampling pattern plays a crucial role with the present of these artifacts, because the result is than convolved with the point-spread-function (PSF) of the sampling pattern.

In compressed sensing, incoherent sampling patterns are beneficial, because then the PSF is noise-like. Therefore, choosing sampling points randomly turns the reconstruction in to a de-noising problem. Nevertheless, the main information of the image is in the low frequencies of the k-space. Therefore it is advantageous to fully sample the k-space center. This set up is also called uni-density sampling pattern.

The PSF of the incoherent sampling can be further improved by using a Poisson-disk distribution of the sampling points. The Poisson-disk distribution is an incoherent sampling pattern were the sampling points have similar distances to each other, producing a blue noise characteristic [7]. Furthermore, changing the density of sampling points in a function of the distance to the k-space center produce a sampling pattern proposed by Lustig et. al. [23].

A non-incoherent sampling pattern has been proposed by Sumpf et al. [37]. Thereby, the k-space is fully-sampled along one dimension and acquired in blocks at different frequencies over the echoes. This sampling pattern is advantageous by reconstructing two-dimensional acquisitions, because the measurement along the read-out direction is a simple ADC. Meaning, down-sampling along the read out direction is not decreasing the acquisition time. The disadvantage of the block sampling scheme is the fewer k-space coverage and its PSF causing ghosting along the phase-encoding direction despite no convolution along the read out direction.

These three sampling patterns have been implemented in the frame-work of the model-based iterative reconstruction and it is possible to easily switch between them. Figure 3.3 illustrates the different by the framework generated sampling-patterns and their corresponding PSF.

## 3.4 Sequence Parameter Optimization

First, a numerical phantom simulating a GRE dataset has been used in order to explore the sensitivity to noise. This phantom has compartments of varying T2* and proton-density values. Furthermore artificial field inhomogeneity is applied and it can be corrupted with complex noise at an arbitrary SNR. The parameter maps of the numerical phantom with different SNR have been reconstructed using the model-based iterative reconstruction and the standard pixel-by-pixel fitting approach on fully sampled data. These two outcomes have been compared to each other assessing the noise

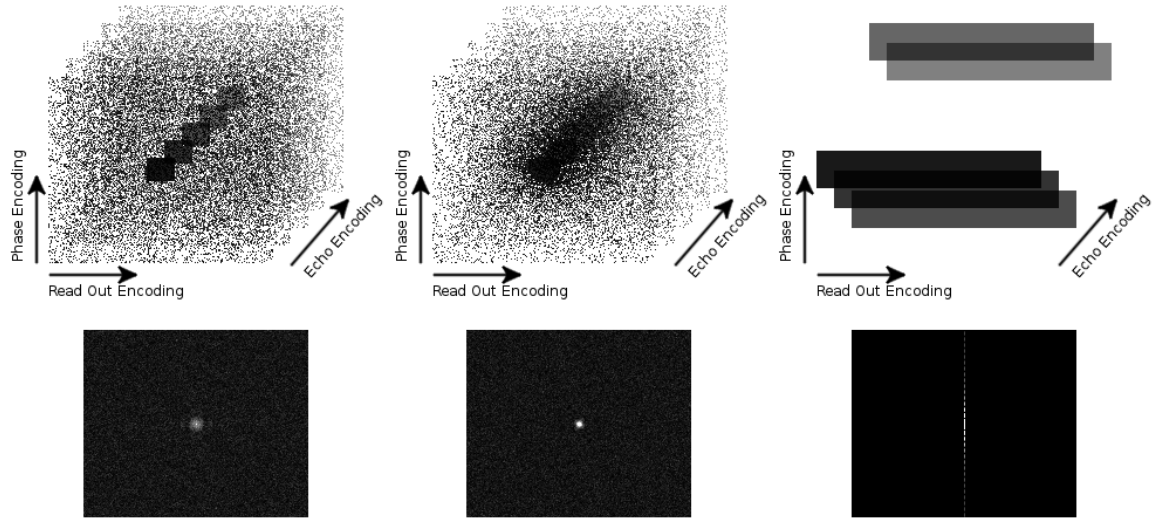


Figure 3.3: Different sampling patterns (top) and its corresponding PSF(bottom) at an acceleration factor of five. The uni-density pattern (left), poisson-disk distribution with a higher sample-density in the k-space center(middle) and the block-sampling pattern(right).

sensitivity.

The in-vivo data has been acquired in several sessions on a 3T clinical scanner (Magnetom Trio a Tim System, Siemens Healtcare, Germany) with healthy volunteers in the Centre Hospitalier Universitaire Vaudois (CHUV). An informed consent of each volunteer has been obtained. Thereby several datasets with differing sequence parameters have been acquired in order to explore an ideal setting for the model-based reconstruction. Two-dimensional datasets with different bandwidth, number of echoes, maximum TE and flow-compensation have been acquired. The datasets have been measured fully sampled and artificial under-sampled off-line. This allows to compare the iterative reconstruction to a standard pixel-by-pixel fitting approach on fully sampled data. The comparison is performed using absolute difference images, a normalized-root-mean-square-error (NRMSE) and a structural similarity measurement (SSIM). The NRMSE is defined as follows,

$$\begin{aligned} RMSE(g,f) &= \sqrt{\frac{\sum_i (g_i - f_i)^2}{n}} \\ NRMSE(g,f) &= \frac{RMSE(g,f)}{f_{max}}. \end{aligned} \tag{3.18}$$

Where $f$ denotes a reference image, $g$ the image which needs to be evaluated and $n$

the number of pixels. In this project, $f$ is the outcome of the standard fitting approach and $g$ the outcome of the model-based iterative reconstruction.

The SSIM is an algorithm analysing the structural similarity between two images, thereby a SSIM-value of one denotes identical images and a SSIM-value of zero different images [40].

## 3.5 Scanner Implementation

To explore the technical feasibility of iterative model-based reconstruction, a part of the project is dedicated to integrate the T2-mapping iterative algorithm (real-valued signal model) on a clinical MR scanner platform (Magnetom Trio a Tim System, Siemens Healtcare, Germany) and optimize it for clinical application.

### 3.5.1 Platform Integration

First, the algorithm needs to be implemented in the programming language C++ in order to integrate it into the scanner environment. This has been realised by replacing step by step MATLAB functions with C++ functions and constantly evaluating the accuracy by comparing to the MATLAB reconstruction outcome. Furthermore, frameworks needed to be evaluated to replace standard MATLAB operations, such as non-linear fitting and Fourier-transform. The pixel by pixel non-linear fitting for the initial-guess has been replaced by a Levenberg-Marquart fitting [27] from the GNU Scientific Library (GSL)[8]. The "Fastest Fourier Transform in the West." (FFTW) framework [12] is used in order to perform the Fourier transforms in the C++ implementation.

Finally, the resulting C++ algorithm and its frameworks need to be compiled in the scanner framework and connected with the reconstruction-chain. The connection to the reconstruction-chain is realized by using a compressed-sensing framework. This framework calls the iterative reconstruction in parallel for each measured slice and provides the measured k-space, a binary mask indicating the sampling pattern and coil sensitivity maps.

### 3.5.2 Performance Optimization

Model-based iterative reconstruction is known to be computational expensive. The first version of the reconstruction in the scanner environment was performed in three hours computation for a whole brain scan. Such a long reconstruction time is not acceptable in clinical routine and performance optimizations need to be done in order to reach the acceptance of clinicians.

The optimization algorithm mainly performs the functions to calculate the cost and the gradients of the cost. Thereby, the bottle-neck of the computational cost is the

Fourier transforms within these functions. Furthermore, the performance strongly depends on the matrix-size of the image volume. Hence, the main goal of the performance optimization is to reduce the complexity of the Fourier transform, matrix size and number of iterations.

The complexity of the Fourier transform can be reduced by using an advantage of the block-sampling pattern. As explained in Section 3.3, the readout direction is fully sampled. Therefore, a inverse Fourier transform of one line is not effected by under-sampling artifacts, thus calculating the residuum along a line in image space is valid. This means, a Fourier transform along the read-out direction is not necessary, it is only necessary along the phase encoding direction where under-sampling artifacts occur. Consequently, every performed two dimensional Fourier transform become one dimensional, hence halving computational cost without changing the outcome.

The matrix size can be reduced by combining redundant information of the coil-elements. In this project, a Principal Component Analysis (PCA) has been used to reduce the number of coil-elements by compressing them to virtual coil-elements. It has shown that compressing from 32 to eight coil-elements, yield the same results and reducing the computational cost by a factor of four.

The number of iterations can be reduced by introducing more sophisticated stop criteria besides reaching the maximum of iterations or a usually too low tolerance. In this project a convergence test has been introduced provided by the C-implementation of the CG-descent optimizer.Thereby, the optimizer can assume that the solution has been reached if after several iterations the cost-function value $\phi$ has not changed [18]. Introducing this test causes the performance to be image content dependent. For example, a noiseless image converges much faster than a noisy image, thus requires less iterations.

# 4 Results

## 4.1 Reconstructing Gradient-Recalled-Echo Data

Figure 4.1 shows that reconstructing GRE data with a real-valued signal model clearly suffers from system related and biological effects, hence fails to reconstruct the parameter maps. T2* values are highly underestimated at the boundaries of the brain, areas where field inhomogeneities occur, hence the signal is complex. This proofs the necessity to model a complex-valued signal.

Reconstructing using the complex-valued signal model yield the desired parameter maps, as shown in figure 4.2. The field map and initial-phase map contains areas of high values in contrary to the reconstruction of MSE data (Section 4.2). These areas are at typical locations for field inhomogeneities and consist of frequency shifts with more than 20Hz and an initial-phase of more than $\frac{\pi}{2}$.

Figure 4.3 shows the reconstruction performed with different down-sampling factors. The reconstructions on two and three times under-sampled data yield T2* maps with less than 3ms difference to the fully sampled reconstruction. Further increasing the acceleration introduce noise in the resulting parameter-maps. The reconstruction with a under-sampling factor of eight and higher produce non-acceptable T2* maps with areas containing more than 10ms differences to the reference.

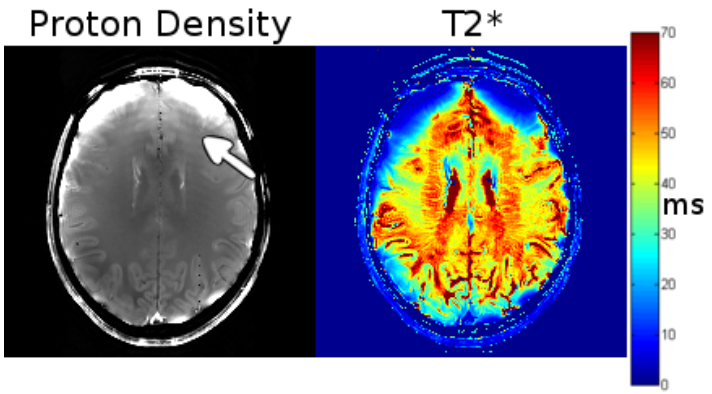


Figure 4.1: The iterative reconstruction with a real-valued signal model performed on a GRE dataset. The used dataset is three times under-sampled. The reconstruction clearly fails to reconstruct the proton-density(left) and T2* map (right). The proton density suffers from strong aliasing artifacts due to the PSF of the block-sampling (arrow). The T2* map contains unrealistic values close to zero, escpecially at the boundaries of the brain.

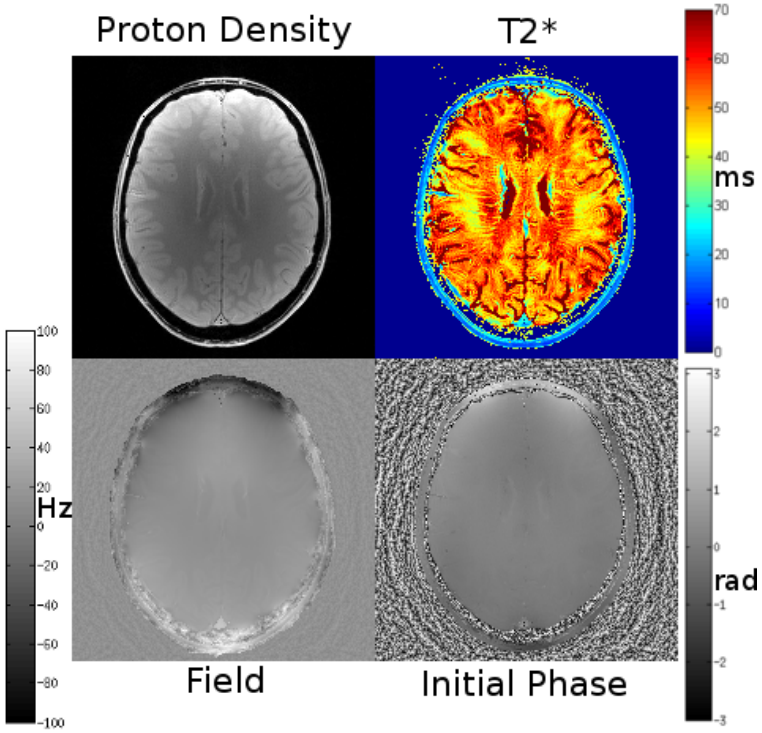


Figure 4.2: The iterative reconstruction with a complex-valued signal model performed on a GRE dataset. The used dataset is three times under-sampled. The resulting parametermpas for proton density(top left), T2* (top right), field inhomgenity (bottom left) and initial-phase (bottom right) contain expected values.

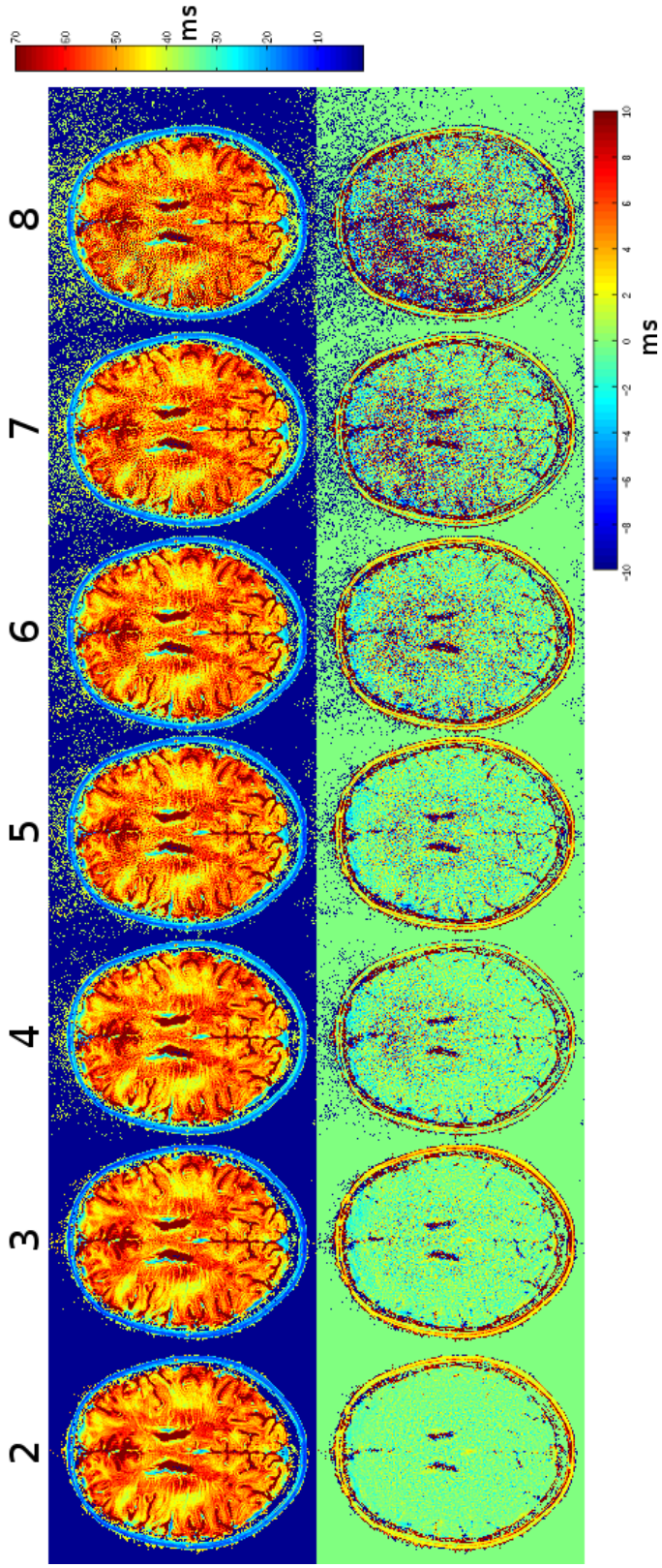


Figure 4.3: The iterative reconstruction, using a complex-valued model, applied on a the same dataset with different under-sampling factors. The resulting T2* maps are shown in the top row. The absolute difference to the reference, reconstruction on fully sampled data, is shown in the lower row. Thereby, the difference to the reference increases with higher down-sampling.

### 4.1.1 Regularization

Theoretically, regularizing the field-map and initial phase should reduce the noise in the resulting parameter maps. Therefore, several reconstructions with different acceleration factors and a regularization of the field map and initial phase has been performed. Figure 4.4 plots the resulting NRMSE/SSIM in function of the acceleration factor for both regularized and non-regularized reconstruction. This shows that no regularization is needed with down-sampling factors up to four to yield good results. Actually, the results with regularization at these down-sampling factors show a systematic increase of the T2* values, due to suppressing the optimizers freedom. However, reconstructing with regularizations at under-sampling factors higher than four show better results. Furthermore, the introduced error when using regularization is smoothing instead of noise. Meaning T2* mean values in a region are preserved, just structural details vanish. This effect is noticeable when comparing the resulting T2* maps of regularized and non-regularized reconstructions in Figure 4.5.

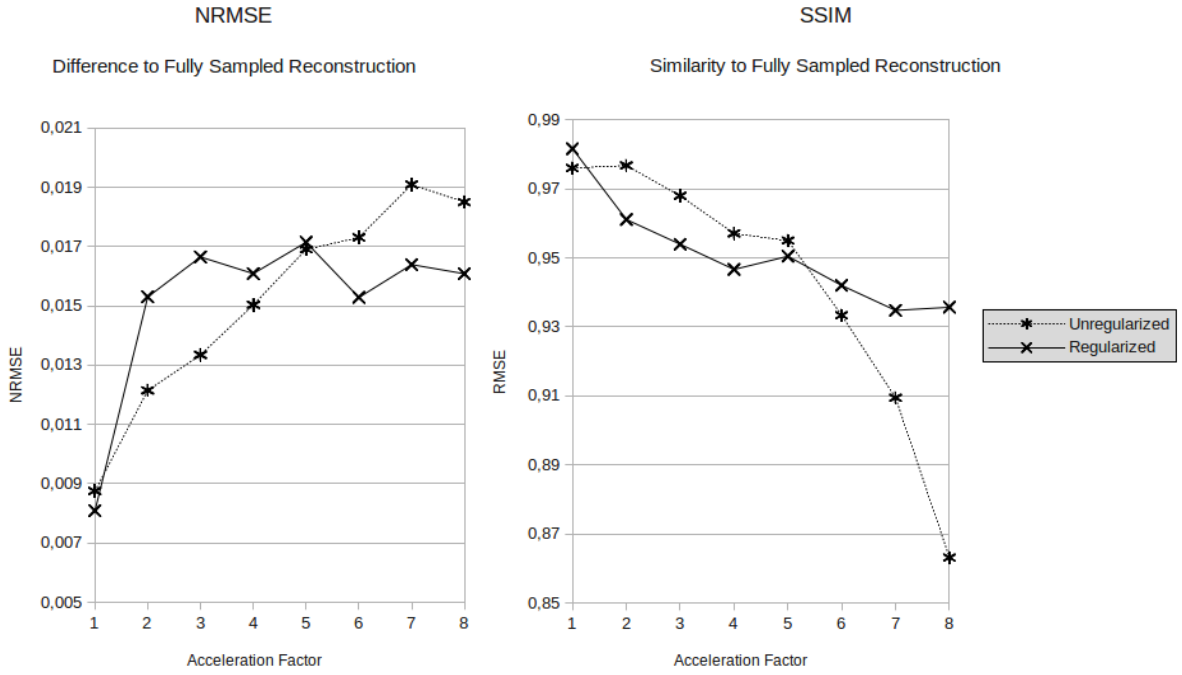


Figure 4.4: The NRMSE (left) and SSIM(right) to a standardfitting approach of a regularized and unregularized reconstruction in function of the acceleration factor.

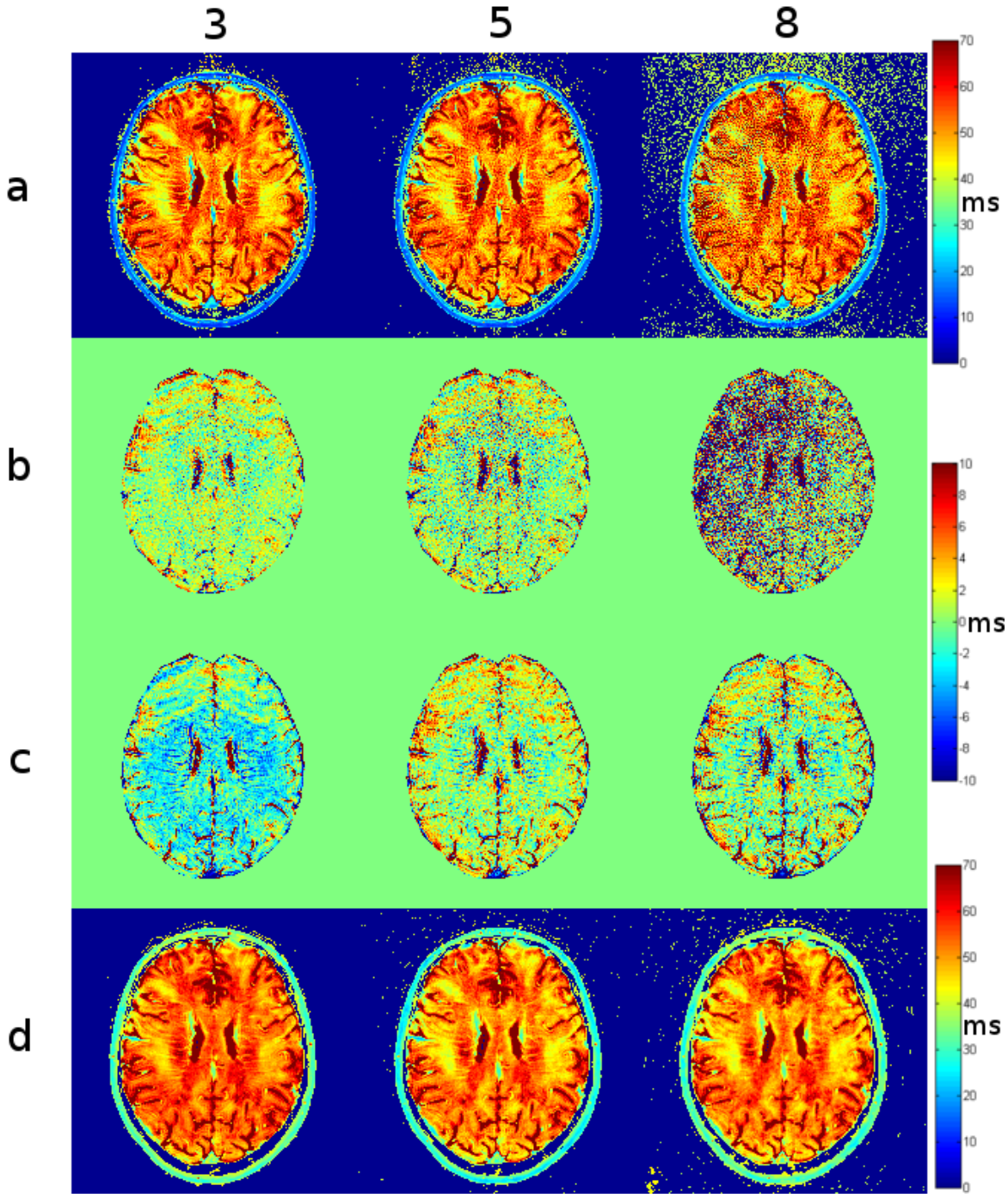


Figure 4.5: Reconstructions, without(row a) and with regularization (row d). The absolute difference to the standard fitting approach is shown in row b(unregularized) and row c(regularized).

### 4.1.2 Sequence Parameter Optimization

The effect of different acquisition parameters of the GRE sequence on the outcome of the model-based iterative reconstruction is presented in this section. Thereby the complex-signal model has been used throughout.

First, a numerical phantom has been used in order to determine the sensitivity to noise of the model-based iterative reconstruction. Thereby, the T2* map was reconstructed by using both a standard fitting approach on fully sampled k-space and the model-based iterative reconstruction on two times under-sampled k-space. The underlying T2* values are known and the fitting error can be directly calculated by using it as reference. Figure 4.6 shows, decreasing the SNR understandably increases the NRMSE of both algorithms. Furthermore, it shows, that the model-based reconstruction is more sensitive to the SNR, because its difference to the reference is constantly higher than the standard fit. Additionally, the presents of single pixels with highly underestimated T2* values increases with decreasing SNR. This effect increases with higher acceleration factors. Figure 4.7 shows a subset of T2* maps from this experiment, indicating the pixel errors with arrows.

The assumption that introducing noise into the in-vivo data by increasing the bandwidth can be proven by looking at the background noise in the proton density and the variance of T2* values. Figure 4.8 shows this background noise of three measurements, using different bandwidths (300Hz,720Hz,1180Hz). Unfortunately, the 300Hz measurement contains slight motion artifacts, visible by ghosting along the phase encoding direction (vertical). However, it shows that more noise is present in the outcome with increased bandwidth. This can be further proofed with figure 4.9, showing a plot of the T2* value variation within a region of interest containing white matter. Both sampling patterns, Poisson- and block-sampling show the least variance with a bandwidth of 300Hz, despite the motion artifacts. The variance of the block sampling is generally lower because its PSF cause low frequency ghosting, not noise as the PSF of the Poisson-sampling pattern.

To illustrate the effect of decreasing the number of echoes an experiment has been conducted where the number of echoes of one dataset is artificially reduced from 32 down to four and a model-based iterative reconstruction performed with both Poisson- and block-sampling pattern. The results are compared to a standard fitting approach on fully sampled data using absolute difference images and the NRMSE. The NRMSE plot in Figure 4.10 shows, the error increase linear by reducing the number of echoes when using a block-sampling pattern. Thereby the error spreads according to the PSF along the phase-encoding direction(vertical). In contrary, the Poisson-sampling pattern appears to be more robust when decreasing the number of echoes. The error of the outcome starts to increase when using less than 16 echoes and is in general lower than the error of the block-sampling pattern. Figure 4.11 shows the resulting T2* maps of both Poisson-sampling block-sampling using different number of echoes. The corresponding difference images to the reference confirm the assumption that Poisson sampling pattern

is more robust in performing on less echoes than the block sampling pattern.

Another important aspect is to decide how long to sample after the excitation. This length influence the coverage of the decay by sample points, thus has a strong impact on the accuracy of the model-based iterative reconstruction. Therefore one dataset with a good coverage (maximum TE: 100.7ms) has been acquired. Afterwards, echoes have been removed step by step, hence the coverage reduced and a model-based iterative reconstruction performed. Results are the parameter maps reconstructed on samples with different coverage of the decay. Figure 4.12 shows a subset of these reconstructions with a maximum TE of 22.7ms, 68.6ms and 100.7ms. There is no obvious difference between the reconstruction with a maximum TE 100.7ms and 68.6ms. However, the reconstruction with maximum TE of 22.7ms is extremely sensitive to noise because it only covers the very begin of the decay which appears more linear than exponential, so that outliers have a huge impact on the resulting T2* value.

To demonstrate the effect off susceptibility Figure 4.13 shows a slice above the nasal-cavity. An anatomic location with strong susceptibility. This location has been acquired on the same volunteer with different slice thickness's(4mm,3mm,2mm) and an identical in-plane resolution(1mm x 1mm). It clearly shows, that decreasing the voxel size decreases the effect of susceptibility, because the T2* values at the nasal-cavity get longer, thus into an expected normative range. However, the SNR decreases as well, visible as a decreasing intensity in the proton density.

To illustrate the effect of flow compensation, Figure 4.14 shows slices of two datasets. One of this datasets is acquired with flow compensation turned on and the other with the same acquisition parameters except flow compensation turned off. On the first glance, there is no obvious difference. However, vessels occur with a higher intensity in the proton density.

Finally, out of this experience, a three-dimensional dataset has been acquired with low bandwidth (300Hz), 16 echoes within 70ms after excitation and small voxel-size (1.6mm x 1.6mm x 1.6mm). The complex-valued model-based iterative reconstruction has been used to reconstruct the parameter maps. Figure 4.15 shows a subset of slices from this reconstruction. For more details of the acquisition parameters see appendix 7.2.2.

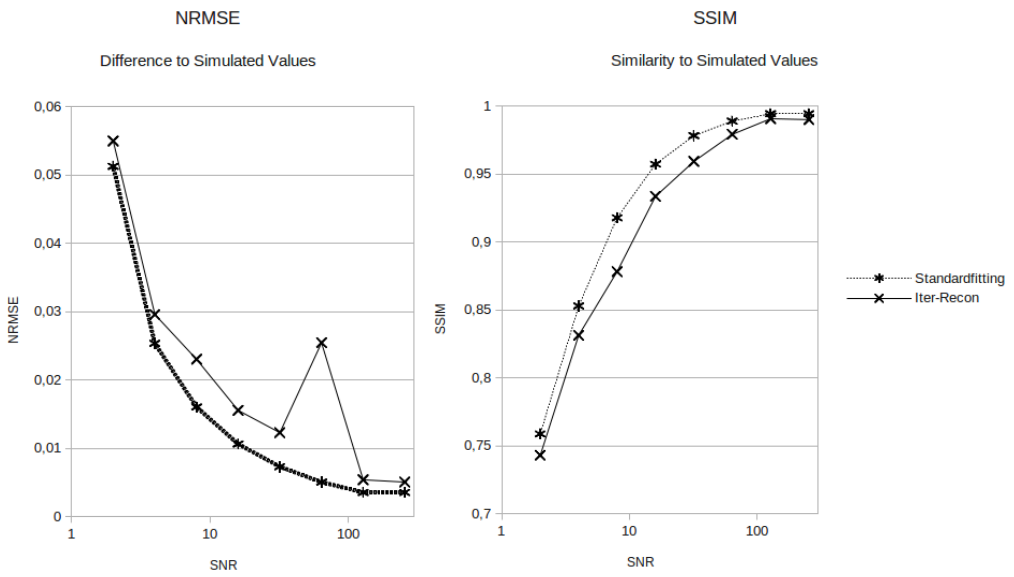


Figure 4.6: Plots of the NRMSE and SSIM(left) to the simulated T2* map, in a function of SNR.

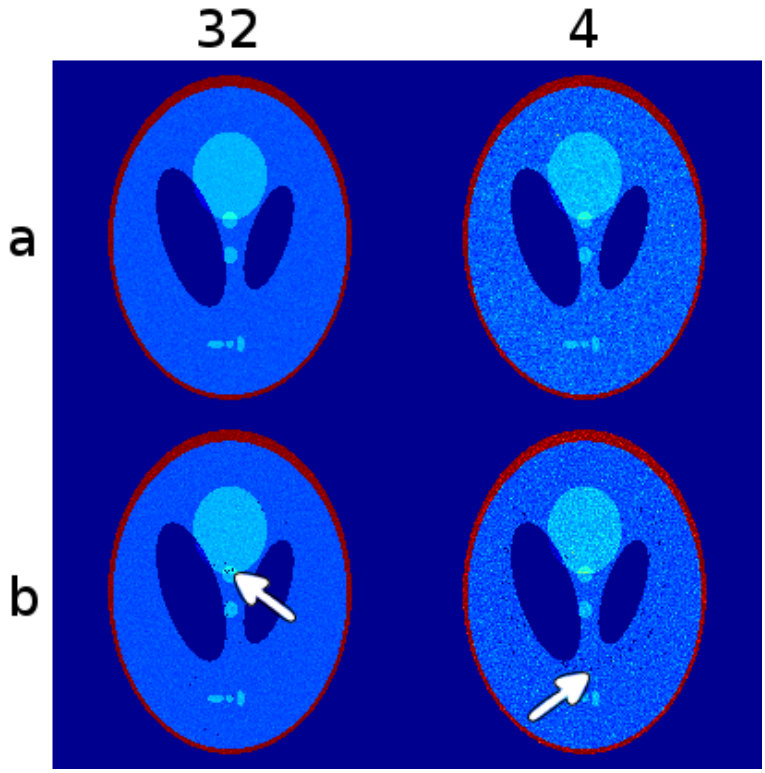


Figure 4.7: Resulting T2* maps of the standard fitting approach(row a) and model-based iterative reconstruction (row b) with a SNR of 32 and four. The arrows indicate single pixels which have been failed to reconstruct.

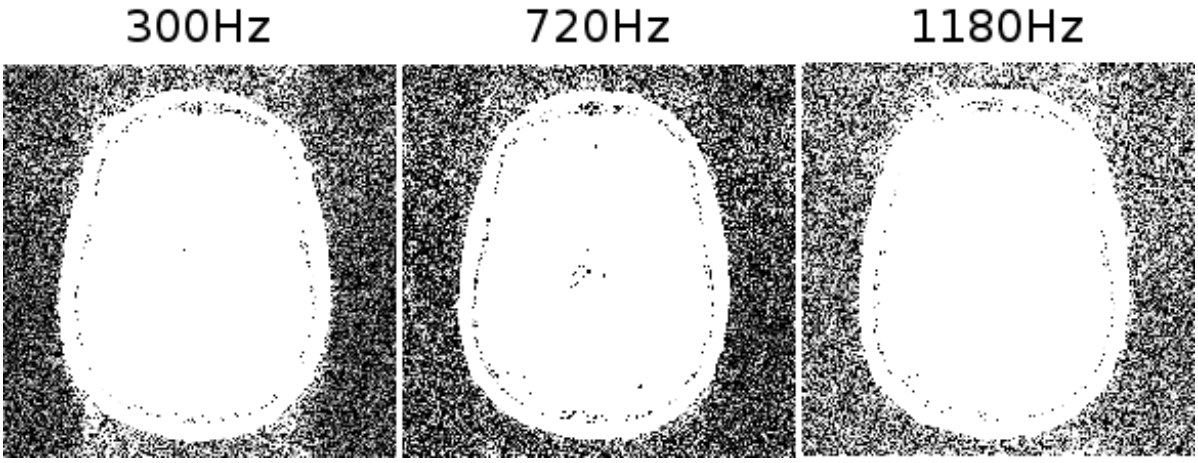


Figure 4.8: Background noise in the proton density of datasets acquiered with a bandwidth of 300Hz(left), 720Hz(middle) and 1180Hz(right).

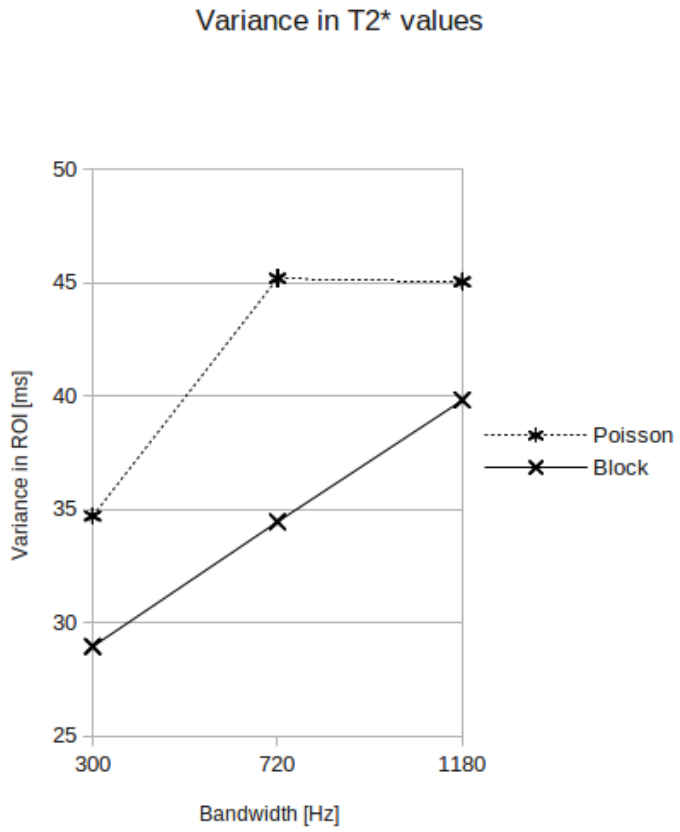


Figure 4.9: Variance within a region of intrest(ROI) containing white matter in the T2* map in function of the bandwidth.

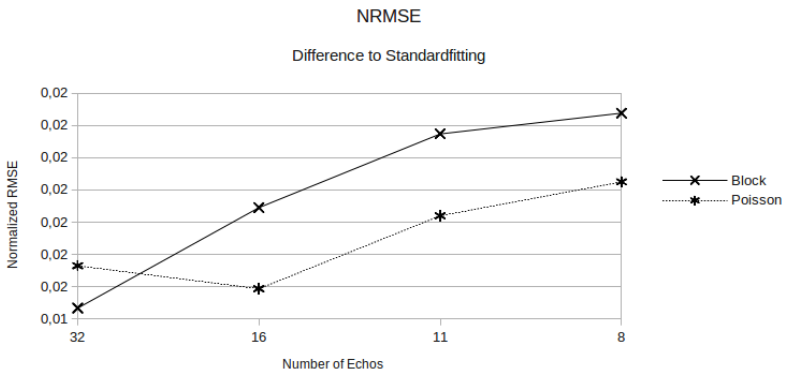


Figure 4.10: A plot of the NRMSE to the standard fitting approach (using 32 echos) in a function of used echos.

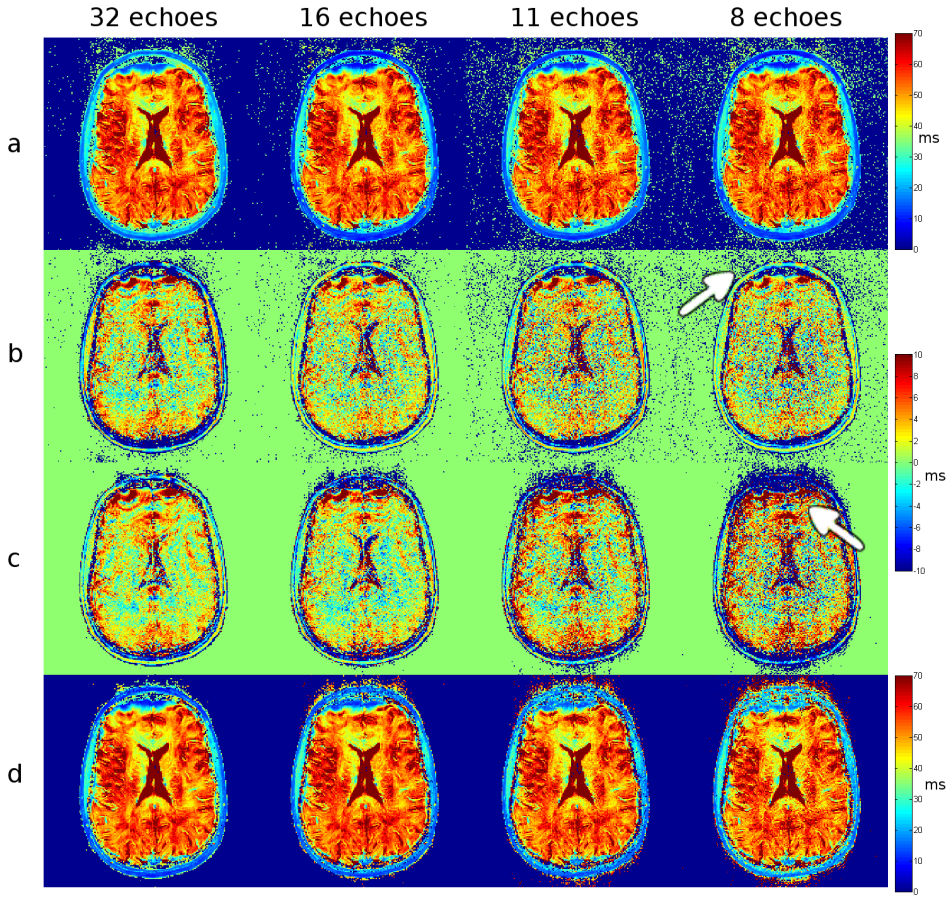


Figure 4.11: Resulting T2* maps(right) using a Poisson sampling (row a) and its corresponding difference map (row b). Furthermore the T2* maps using a block-sampling (row d) and its corresponding difference map (row c). Thereby the error increases by decreasing the number of echoes and spreads according to the PSF of the sampling-patterns(arrows).

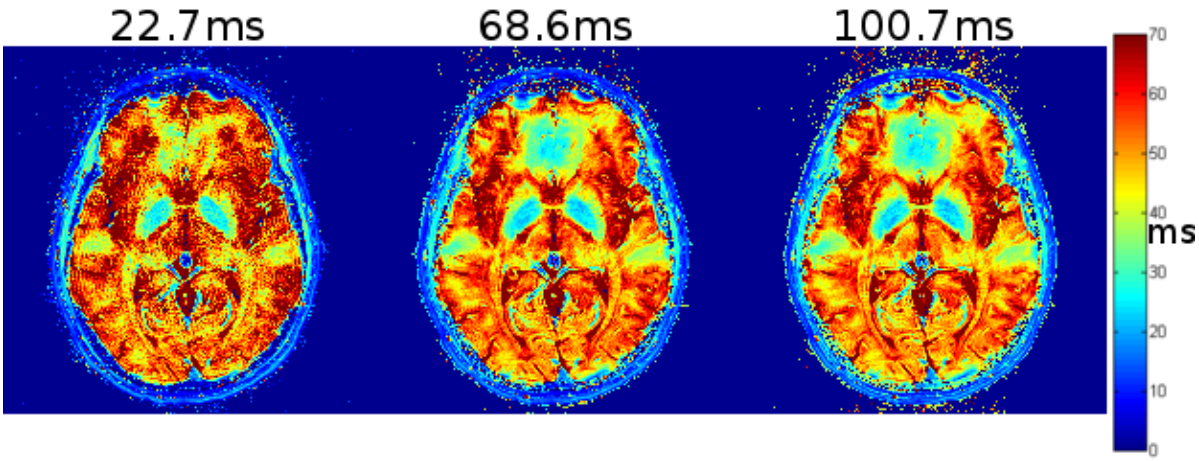


Figure 4.12: T2* maps of model-based reconstructions of the same dataset with different maximal TE. Thereby the presence of noise increases with a shorter maximal TE.

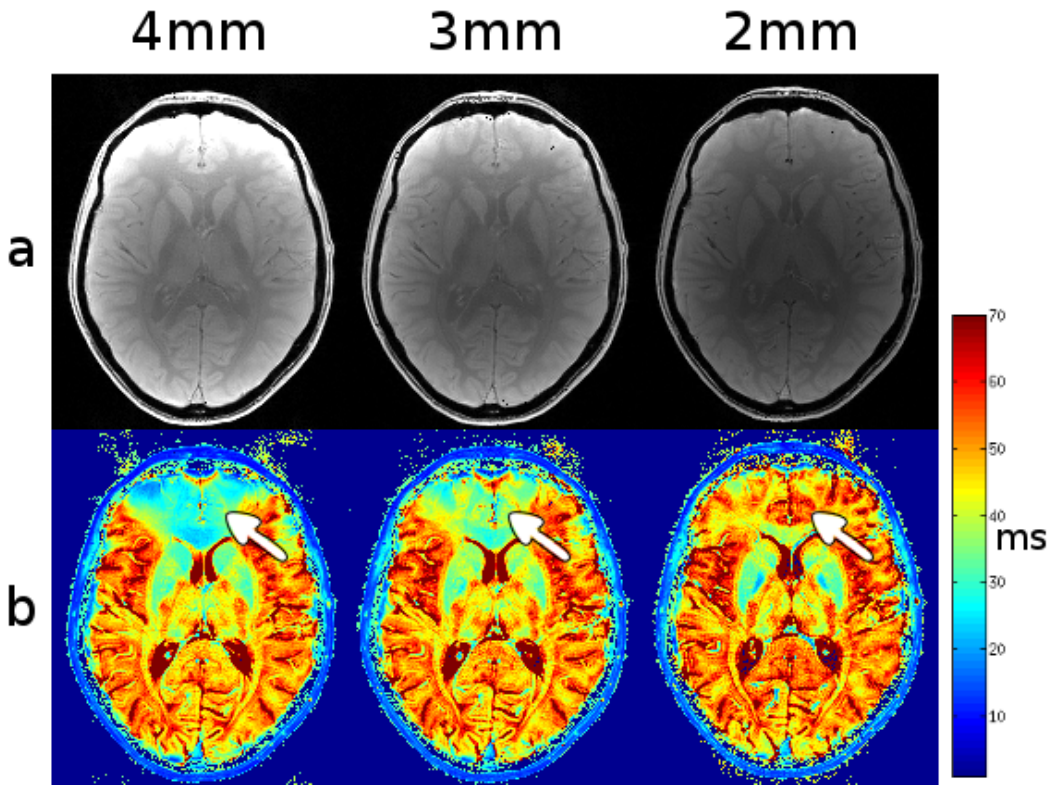


Figure 4.13: Three aquisitions on the same volunteer but different slice-thickness (4mm,3mm and 2mm). In row a) the resulting proton-density maps and in row b) the reconstructed T2* maps with decreasing suscebtibility(arrows) by decreasing slice thickness. The reconstructions were performed on three-times undersampled datasets without regularizations. Thereby, the windowing for each three datasets is the same.

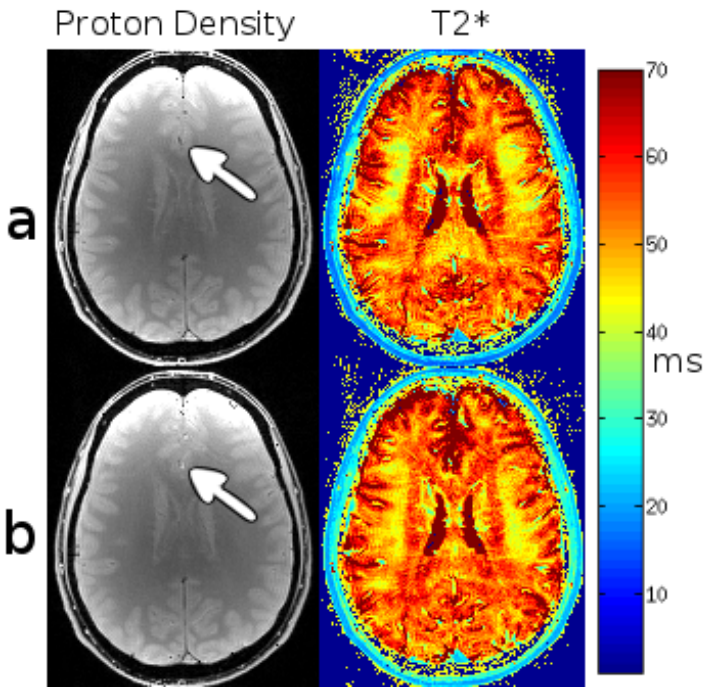


Figure 4.14: A slice of the same volunteer measured without(row a) and with flow compensation(row b). Thereby the only visible difference is the higher intensity of vessels with flow compensation (arrows).

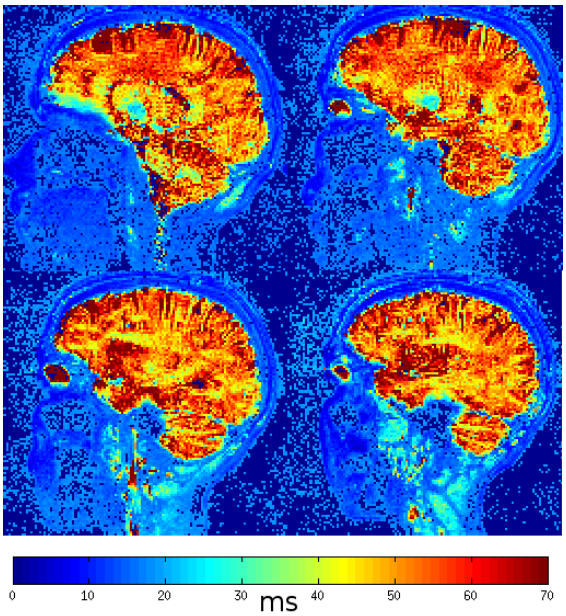


Figure 4.15: A subset of slices within the T2* map, reconstructed on a three dimensional, three times undersampled dataset, without regularizations.

## 4.2 Reconstructing Multi-Spin-Echo Data

Iterative reconstruct a MSE dataset with the real-valued signal model has already proven to work robustly by Sumpf et al. [37]. Figure 4.16 shows the resulting parameter maps of a reconstruction on a five times under-sampled dataset. Thereby the block-sampling pattern was used.

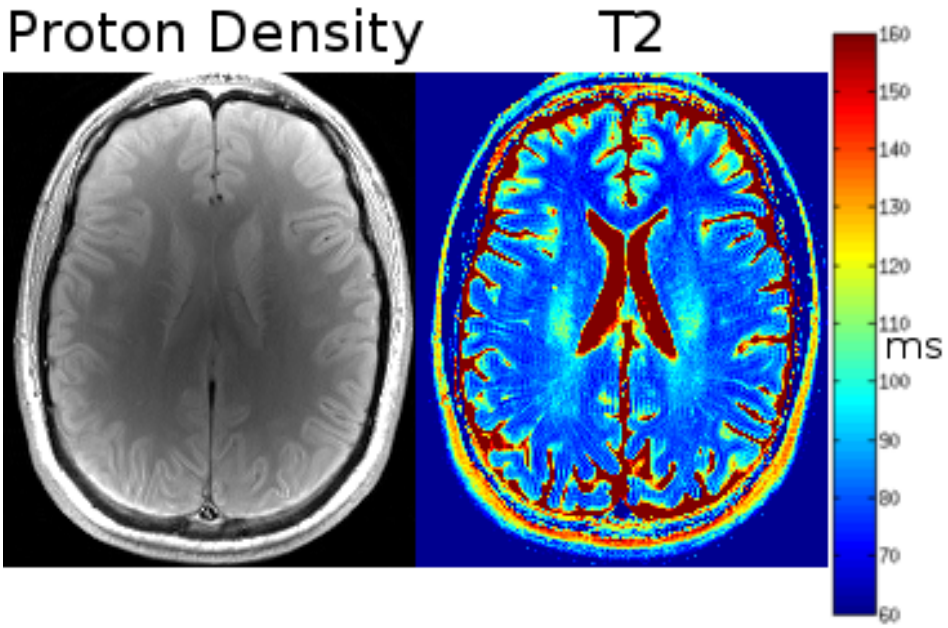


Figure 4.16: The iterative reconstruction with a real-valued signal model performed on a MSE dataset. The used dataset is five times under-sampled and the proton-density (left) and T2 map (right) contain expected values.

Iterative reconstruct a MSE dataset with a complex-valued signal model produce good results as well. Figure 4.17 illustrates the four resulting parameter maps of a reconstruction on a five times under-sampled dataset. Thereby the Poisson-sampling pattern was used. However, the T2 values are about 3 milliseconds higher than in the real-valued reconstruction. Furthermore, the initial phase and field map is close to zero, except at vessels due to phase effects caused by blood flow.

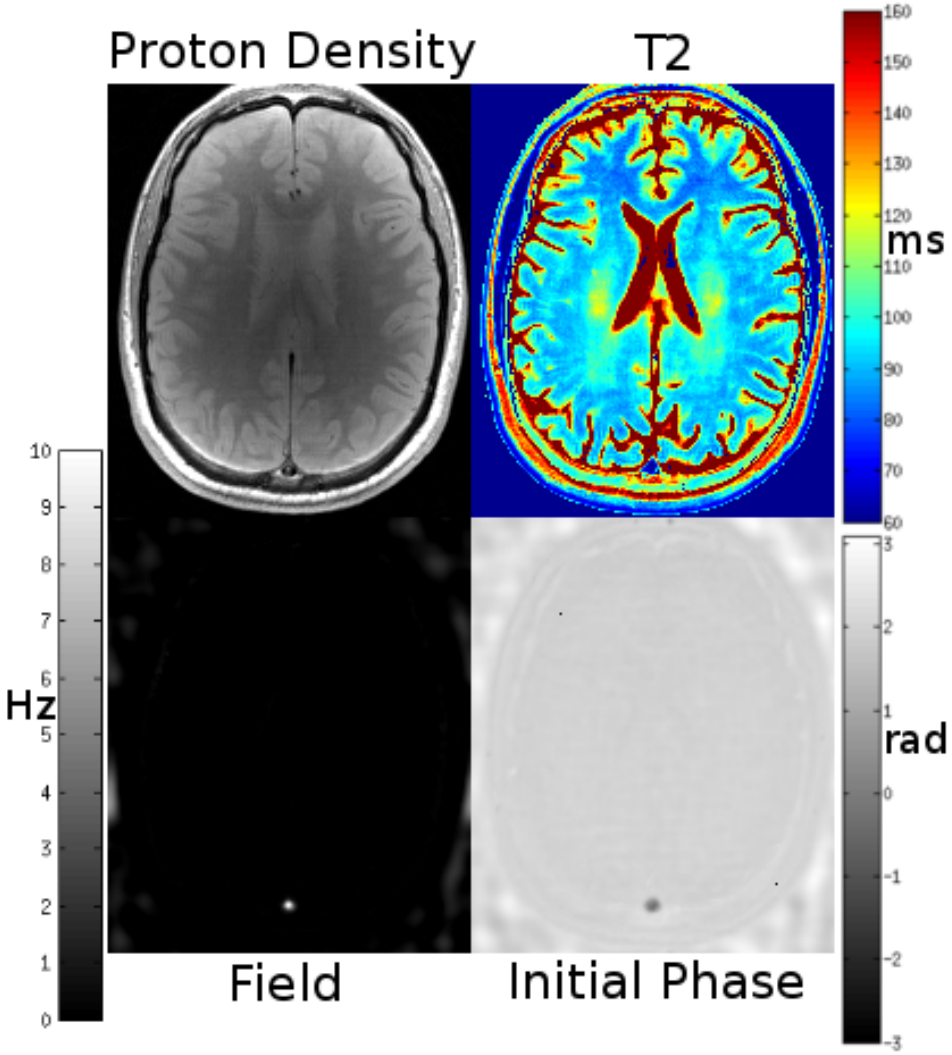


Figure 4.17: The iterative reconstruction with a complex-valued signal model performed on a MSE dataset. The used dataset is five times under-sampled and the proton-density (top left) and T2 map (top right) contain expected values. The parameter maps for field inhomogenity (bottom left) and initial phase (bottom right) contain values close to zero.

## 4.3 Scanner Implementation

The implementation of the C++ function yields similar parameter maps as the MATLAB implementation. Figure 4.18 shows the resulting parameter maps of the provided MATLAB algorithm and the C++ implementation. Effectively, the result of the C++ algorithm is smoother than the MATLAB version. The reconstruction with the MATLAB algorithm needs a computational time of 2 minutes 31 seconds on a Windows 7 machine (Intel(R) Core(TM) i7-3770K CPU @ 3.50GHz, 16GB RAM). Thereby the

reconstruction of the same dataset using the C++ implementation after performance optimization requires 36 seconds on the same machine. The performance however strongly depends on the image content, and may vary between 30 seconds and 3 minutes.

The integration of the algorithm in the scanner-environment reconstructs a full brain scan with 30 slices within around 12 minutes. After reconstruction, the parameter maps are saved as DICOM files and can be reviewed at the scanners user interface, as shown in figure 4.19.

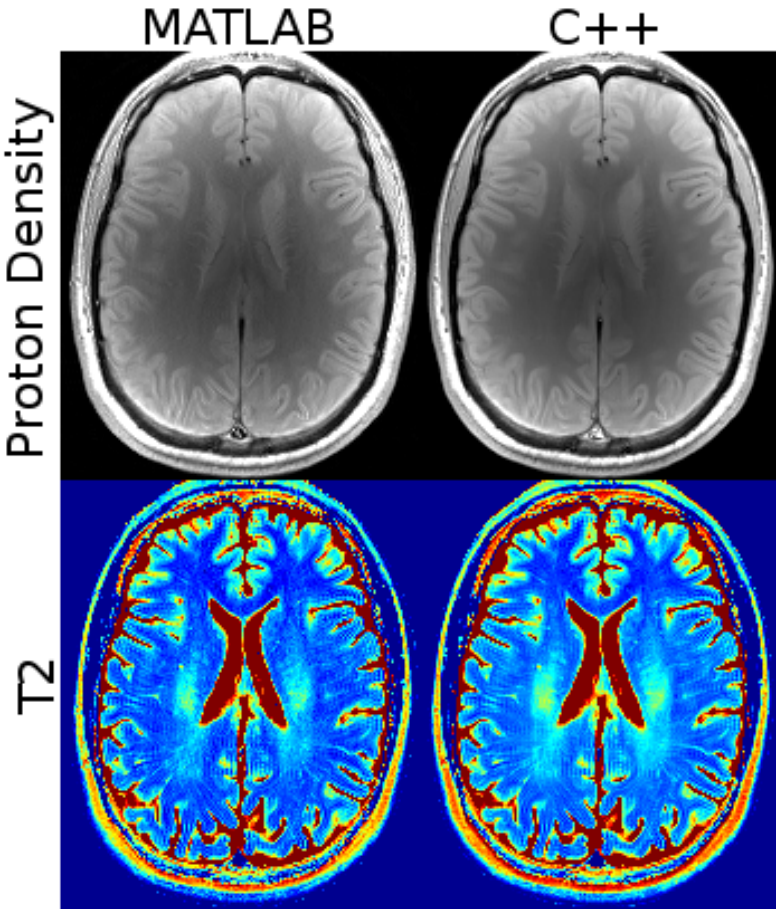


Figure 4.18: The resulting parameter maps, proton-density(top) and T2 (bottom), in comparison of the MATLAB algorithm (left) and C++ implementation(right).

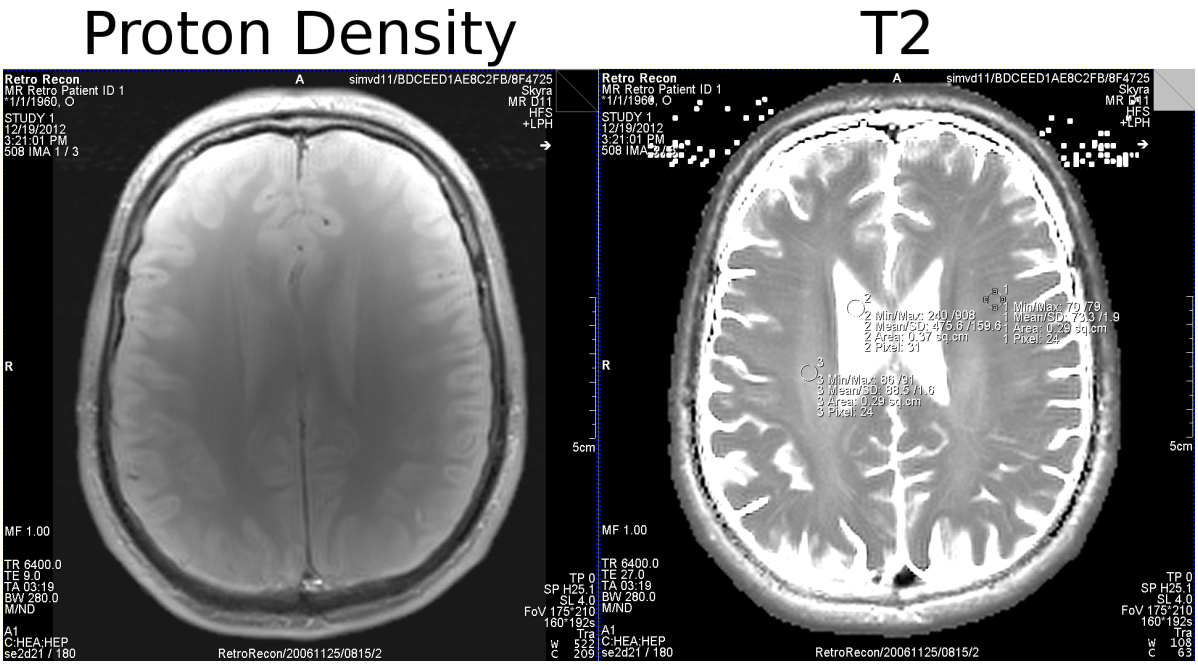


Figure 4.19: The resulting parameter maps, proton-density (left) and T2 (right), from the algorithm integrated in the scanner system.

# 5 Discussion

## 5.1 Iterative Model-Based Reconstruction for T2* Mapping

As shown in the results, the phase of an image acquired with a GRE is not negligible. Therefore the complex-valued signal model needs to be used in order to deal with system related and biological effects.

In doing so down-sampling factors up to three were found to work robustly without strong noise on the resulting T2* maps. Higher down-sampling factors suffer from increasing noise-like artifacts in the parameter maps, which would render these results unusable for clinical applications. These errors mainly occur from noise in the estimation of the field and initial phase map. The source of this noise may be the phase of the coil sensitivity maps, which are estimated a priori and used as a fixed parameter in the reconstruction. This error increases with higher down-sampling factors and is a potential for improvement in future. However, the field map and initial phase are expected to be smooth, thus applying a regularization as explained in Section 3.2 is a good first approach to deal with that problem.

The advantage of using the regularization is the smooth instead of noise-like appearance of errors, as presented in the results Section 4.1.1. This implies that the ultimate application may determine an "optimal" down-sampling factor. Meaning, applications which require detailed structural information can be acquired with moderate acceleration factors such as three or four and no regularizations. Applications with interest in mean-values of regions could be reconstructed with high acceleration factors such as eight and simultaneous use of regularizations to suppress noise type artifacts resulting in smoothed image information instead but allowing for higher accelerations.

Regularizing the proton density $\rho$ and T2* map using any kind of Total Variation (TV,TV2,TGV) has been discarded in this work, because the effect of removing pathological image content (e.g. lesions) can not be studied with the acquired datasets on healthy volunteers. Furthermore, it is difficult to find a general weighting factor which is always applicable. Meaning, in some slices a high weighting value is required to notice an influence of the regularization, whereas the same weighting value has a large impact within another slice. Finally, such a regularizations tends to lower the robustness of the whole algorithm by suppressing the freedom of the optimizer with to much penalties.

### 5.1.1 Sequence Parameters

The acquisition protocol and the resulting data provided to the reconstruction has a huge impact on the qualitative outcome of the algorithm. Therefore this thesis aimed at exploring the influence of relevant sequence parameters on the performance of the iterative model-based reconstruction in order to yield an optimized imaging protocol for a whole brain T2* mapping application.

First, the SNR sensitivity of the iterative model-based reconstruction has been investigated. The results show that the reconstruction is fairly sensitive to noise. This means, the SNR should be as high as possible, i.e. we found that the SNR should be higher than 10. The following Imaging parameters allow to modulate the SNR: the bandwidth should be as low as possible and the voxel size as big as possible. However, low bandwidth forces the sequence to have a large echo-spacing, thus large spacing between sampling points on the exponential decay. Therefore, the algorithm need to perform with less echoes as possible. Furthermore, large voxel sizes introduce stronger susceptibility artifacts and degrades the spatial resolution. A trade-off between those three parameters(bandwidth,echo-spacing,voxel-size) needed to be found.

The results from reconstructing with different numbers of echoes show, that the quality of reconstruction using a block-sampling pattern strongly depends on the number of used echoes and requires in a realistic setting at least 32 echoes, whereas the Poisson-sampling pattern robustly works with 16 echoes and more. This can be explained by the better k-space coverage of the Poisson-sampling pattern, which requires less echoes than the block sampling. Therefore, the optimal sequence need to measure at least 16 echoes with the constrain that a Poisson-sampling pattern is used in the reconstruction.

Besides the number of echoes, it is important to have a good coverage of the exponential decay by sampling-points. Theoretically, the decay should be sampled as long as possible to perform a good model-based iterative reconstruction though the noise floor at very long echo times may lead to instabilities in the T2 or T2* estimate. However, long TE sampling prolongs the acquisition time, thus a trade off needs to be found. As explained in Section 2.2, the signal intensity is at 37% at the time point of the T2* value, meaning the slope of the decay is fairly strong at this time point. Therefore, as a rule of thumb, the longest TE should be longer than the expected T2/T2* value. Hence the decay should be sampled for approximately 70ms for the T2* at 3T because we expect T2* values around 60ms inside the brain. The results prove this assumption, because reconstructions with a maximum TE lower than 60ms get more sensitive to noise and reconstruction with a maximum TE higher than 70ms do not show significant improvements.

This set-up of 16 echoes within 70ms yields an approximate echo-spacing of 4.4 milliseconds, allowing the sequence to acquire at a low bandwidth of 300Hz, thus improving the SNR in comparison to a high bandwidth as proposed initially by Windischberger et al. [44]. This gain of SNR with reducing the bandwidth allows to reduce the slice thickness, thus reduce susceptibility effects. Therefore, we found a voxel size of 1mm x

1mm x 2mm to provide stable results and recommend those or similar protocol settings for further investigations. At the same time, it should be noted that an approximate 1 mm resolution is expected and routinely used in a large number of clinical brain exams.

Applying the flow-compensation to deal with effects coming from blood flow did not show strong improvements. Effectively, the benefit of the flow-compensation is not worth the extra scan-time, thus will not be applied in future.

The GRE 2D acquisition is a good tool to explore acquisition parameters and the possibilities of the iterative model-based reconstruction. However, measuring a 3D GRE is more reasonable due to two facts; 1) the SNR gain due to exciting a larger volume and 2) the feasibility to apply a Poisson-sampling pattern during acquisition. Therefore, future work is recommended to focus on reconstructing 3D datasets.

## 5.2 Iterative Model-Based Reconstruction for T2 Mapping

The extended model may also be applied to the fitting of T2 data. When applying this complex-valued signal model, the field map and initial-phase appear to be close to zero, except at vessels. Thus the extended model-based reconstruction is capable to detect flow artifacts. However, the gained image quality in the T2 map is negligible when comparing these results to the outcome of the reconstruction using a real-valued signal model. Therefore, it is more reasonable to use the real-valued signal model, because it depends on less parameters, thus is more robust and enables to reconstruct with good results on even highly under-sampled data. Furthermore, a simpler model performs with a better computational time, because the solution space is much smaller, thus the cost function converges within less iterations . Furthermore the calculation of the cost and gradients per iteration is less demanding. Therefore, the real-valued model as proposed by Sumpf et al. [37] will be the chosen method to reconstruct T2 maps on under-sampled MSE data whereas its importance is clearly demonstrated for the T2* mapping protocol.

## 5.3 Translation of Technology

The high expectations in quantitative imaging for clinical diagnostics motivate the integration of the iterative model-based reconstruction into the MR scanners environment. This integrated reconstruction using the real-valued signal model yield the expected T2 maps without major downs-sampling related artifacts, thus proofs the feasibility to use quantitative mapping on real under-sampled data in a clinical setting.

The in comparison to iterative algorithms fast computational time of 10-15 minutes of this project is only accepted by clinicians if the scan process is not disturbed during the reconstruction process. Meaning, another acquisition can be performed during the

computational demanding reconstruction and a constantly ongoing work-flow is guaranteed.

## 5.4 Future Work

The present work has set a starting point for the application of model-based iterative reconstruction for T2* mapping. The investigations indicate that the use of "optimized" imaging parameters allows the reduction of a number of artifacts or in other words improves the accuracy and robustness of the quantitative mapping results. However, the model-based iterative reconstruction for T2* mapping need to be further improved to be more robust at high accelerations factors. For example, by using a more sophisticated sampling scheme, proposed by Knoll et al. [21], were the density of the incoherent sampling-points is chosen according to the object in the image-space. Another improvement can be archived by investigating in the quality of the coil-sensitivities. For example, by initializing the sensitivity estimate with external reference lines. External reference lines are rapidly, fully sampled lines covering the k-space center, which are measured prior to the acquisition. In general, different methods of coil-sensitivity estimation should be explored in order to evaluate the ideal algorithm for the application of model-based iterative reconstruction.

Additionally, more regularizations should be tested as explained in this thesis. For example the well established Tikhonov regularization[3]. Furthermore, the evaluation of the weighting values $\lambda$ can be improved by using a more structured approach instead of a brute force approach. For example, by analysing the resulting spatial resolution by plotting the full-width-at-half-maximum (FWHM) of the PSF in function of the weighting factor $\lambda$ [13, 10].

Furthermore, in future this project will need to further investigate into performance optimizations of the C++ implementation on the scanner to ease the use and increase the acceptance by clinicians. Further ideas to improve performance are using a pruned Fast Fourier Transform (FFT) and a Graphics Processing Unit (GPU) implementation. A pruned FFT can calculate a subset of the k-space instead of calculating the full k-space and artificial under-sample, thus throwing away data after it was calculated [36]. A GPU implementation would accelerate the reconstruction because those processors are specialised to solve large matrix operations such as the costly FFT. However, the realisation of this optimizations demand major changes in the implementation.

Last but not least, the extension to 3D will allow further improvements due to the higher achievable SNR.

## 5.5 Outlook

The utility of quantitative maps is by far not fully explored. On the contrary, the clinical user (radiologist) is only in the process of understanding the potential and pitfalls of the quantitative MRI results. In future, normative ranges and abnormalities due to pathology will be investigated to ensure the success of quantitative mapping. There are three possibilities to collect such a database. First, large scale cohort studies recruiting controls and patients only for the purpose of quantitative mapping, but they are expensive and time consuming. Second, the quantitative mapping will be an additional measurement of ongoing studies. For example, added to the protocol of a multiple-sclerosis or schizophrenia study. Finally, normative ranges can be accomplished with opportunistic scans, where the patients are scanned in clinical routine and retrospectively used as controls if they do not have a diagnosis. All three methods require a fast application of the quantitative mapping in order to be feasible. The fast measurement is archived with down-sampling but the long reconstruct time is a draw back. Taking this step into clinical research became more feasible with the implementation of the accelerated T2 mapping on the scanner.

The algorithm of accelerated T2* mapping has not reached this point yet. More data needs to be acquired to validate the robust performance of the algorithm. Finally, it needs to be integrated in the scanner environment and follow the T2 mapping into clinical research.

# 6 Conclusion

The first goal, extending the model-based iterative reconstruction to be applicable to a GRE sequence in order to perform quantitative T2* mapping was archived by adding two parameters to the theoretical signal model. An important step was the introduction to consider of the complex nature of the T2*-weighted signal to cope with system related and biological effects. To sum up, we can compute T2* maps with up to eight times under-sampled MRI data using this extended model. However, a regularisation is needed at the highest accelerations to deal with artifacts but a smoothing effect will suppress anatomical details. Applications relying on this anatomical details can use an acceleration-factor of three and a reconstruction without regularizations.

The second part, exploring the acquisition parameter space yielded a two-dimensional standard protocol for T2* mapping. To sum up, an parameter set for a 2D T2* mapping protocol using a model-based reconstruction should have the following parameters as guidelines: 16 echoes within 70ms at a bandwidth of 300Hz. Thereby, the echoes are acquired mono-polar to avoid odd-even effects. The best trade-off between SNR and susceptibility effects is archived with a voxel size off 1mm x 1mm x 2mm. A flow compensation in the sequence does not show a benefit worth the additional measurement time, therefore the recommendation would be to turn it off, avoiding additional gradient load. This protocol proofed to yield robust results, even by the presence of strong field inhomogeneities.

Finally, a quantitative T2 mapping algorithm based on highly under-sampled multi-spin echo data has been successfully integrated in the scanner environment and can be now used at the scanner console. In this context, the algorithm has been optimized in terms of computational cost to increase the feasibility to use it in a clinical setting. This is an important step for quantitative mapping from research to the clinics. It enables clinicians to build up databases and explore quantitative T2 values in healthy controls and patients, which is the first step into clinical research and important to explore the utility of quantitative mapping.

# 7 Appendix

## 7.1 Mathematical Derivations

### 7.1.1 Generalized Derivation of the Cost-Function

A generalized derivation rule for a $l2$-normed cost function (2.14) has been proposed by Block et al.[3] and will be proven in this section.

In the first step, the $l2$-norm needs to be reformulated by its definition in order to simplify the function for a derivation. Thereby, the complex conjugate of a variable $x$ will be denoted as $\overline{x}$.

$$\begin{aligned}
\phi(p) &= \frac{1}{2}\|X(p) - Y\|_2^2 \\
&= \frac{1}{2}\sum_j \sqrt{|X_j(p) - Y_j|^2}^2 \\
&= \frac{1}{2}\sum_j |X_j(p) - Y_j|^2 \\
&= \frac{1}{2}\sum_j |X_j(p) - Y_j||X_j(p) - Y_j| \\
&= \frac{1}{2}\sum_j (X_j(p) - Y_j)\overline{(X_j(p) - Y_j)} \\
&= \frac{1}{2}\sum_j X_j(p)\overline{X_j}(p) + Y_j\overline{Y_j} - Y_j(p)\overline{X_j}(p) - X_j\overline{Y_j}
\end{aligned} \tag{7.1}$$

Now, this equation can be derived by applying the product rule, yielding a basic rule to derive cost functions using the $l2$-norm.

$$
\begin{aligned}
\frac{\partial}{\partial p}\phi &= \frac{1}{2}\sum_j \frac{\partial}{\partial p}X_j(p)\overline{X_j}(p) + X_j(p)\frac{\partial}{\partial p}\overline{X_j}(p) - Y_j\frac{\partial}{\partial p}\overline{X_j}(p) - \frac{\partial}{\partial p}X_j(p)Y_j \\
&= \frac{1}{2}\sum_j (\overline{X_j}(p) - \overline{Y_j})\frac{\partial}{\partial p}X_j(p) + (X_j(p) - Y_j)\frac{\partial}{\partial p}\overline{X_j}(p) \\
&= \frac{1}{2}\sum_j \overline{(X_j(p) - Y_j)\frac{\partial}{\partial p}\overline{X_j}(p)} + (X_j(p) - Y_j)\frac{\partial}{\partial p}\overline{X_j}(p) \\
&= \frac{1}{2}\sum_j 2\Re\{(X_j(p) - Y_j)\frac{\partial}{\partial p}\overline{X_j}(p)\} \\
&= \sum_j \Re\{(X_j(p) - Y_j)\frac{\partial}{\partial p}\overline{X_j(p)}\}
\end{aligned}
\tag{7.2}
$$

### 7.1.2 Cost Function Deriviation of the Complex-Valued Model

In order to derive the cost function using the rule of equation (2.14), the signal model,

$$
\begin{aligned}
x_t(\tilde{\rho}, \tilde{R}, \tilde{b}, \tilde{\varphi_0}) &= \mathcal{F}(M_{\sigma,t}(\tilde{\rho}, \tilde{R})e^{iM_{\theta,t}(\tilde{b},\tilde{\varphi_0})}) \\
&= \mathcal{F}(L_\rho\tilde{\rho}e^{-L_R\tilde{R}t}e^{i(2\pi L_b\tilde{b}t + L_{\varphi_0}\tilde{\varphi_0})})
\end{aligned}
\tag{7.3}
$$

needs to be derived with respect to its parameters using the chain rule,

$$
\begin{aligned}
\frac{\partial}{\partial\tilde{\rho}}x_t &= \mathcal{F}(L_\rho e^{-L_R\tilde{R}t}e^{i(2\pi L_b\tilde{b}t + L_{\varphi_0}\tilde{\varphi_0})}) \\
\frac{\partial}{\partial\tilde{R}}x_t &= \mathcal{F}(-L_R t L_\rho\tilde{\rho}e^{-L_R\tilde{R}t}e^{i(2\pi L_b\tilde{b}t + L_{\varphi_0}\tilde{\varphi_0})}) \\
\frac{\partial}{\partial\tilde{b}}x_t &= \mathcal{F}(L_\rho\tilde{\rho}e^{-L_R\tilde{R}t}i2\pi t L_b e^{i(2\pi L_b\tilde{b}t + L_{\varphi_0}\tilde{\varphi_0})}) \\
\frac{\partial}{\partial\tilde{\varphi_0}}x_t &= \mathcal{F}(L_\rho\tilde{\rho}e^{-L_R\tilde{R}t}iL_{\varphi_0}e^{i(2\pi L_b\tilde{b}t + L_{\varphi_0}\tilde{\varphi_0})})
\end{aligned}
\tag{7.4}
$$

Now, the equations can be simplified by replacing scaled parameters with unscaled parameters ($\rho = L_\rho\tilde{\rho}$, $R = L_R\tilde{R}$, $b = L_b\tilde{b}$, $\varphi_0 = L_{\varphi_0}\tilde{\varphi_0}$),

$$\begin{aligned}
\frac{\partial}{\partial\tilde{\rho}}x_t &= \mathcal{F}L_\rho e^{-Rt}e^{i(2\pi bt+\varphi_0)} \\
\frac{\partial}{\partial\tilde{R}}x_t &= \mathcal{F}(-L_R t\rho e^{-Rt}e^{i(2\pi bt+\varphi_0)}) \\
\frac{\partial}{\partial\tilde{b}}x_t &= \mathcal{F}L_b\rho e^{-Rt}i2\pi te^{i(2\pi bt+\varphi_0)} \\
\frac{\partial}{\partial\tilde{\varphi_0}}x_t &= \mathcal{F}L_{\varphi_0}\rho e^{-Rt}ie^{i(2\pi bt+\varphi_0)}
\end{aligned} \tag{7.5}$$

In the next step, the weighting by coil sensitivities $C_c$ is added.

$$\begin{aligned}
\frac{\partial}{\partial\tilde{\rho}}x_{t,C_c} &= C_c\mathcal{F}(L_\rho e^{-Rt}e^{i(2\pi bt+\varphi_0)}) \\
\frac{\partial}{\partial\tilde{R}}x_{t,C_c} &= C_c\mathcal{F}(-L_R t\rho e^{-Rt}e^{i(2\pi bt+\varphi_0)}) \\
\frac{\partial}{\partial\tilde{b}}x_{t,C_c} &= C_c\mathcal{F}(L_b\rho e^{-Rt}i2\pi e^{i(2\pi bt+\varphi_0)}) \\
\frac{\partial}{\partial\tilde{\varphi_0}}x_{t,C_c} &= C_c\mathcal{F}(L_{\varphi_0}\rho e^{-Rt}ie^{i(2\pi bt+\varphi_0)})
\end{aligned} \tag{7.6}$$

Finally, this equations need to be inserted into rule (2.14), yielding the following deviations:

$$\begin{aligned}
\frac{\partial}{\partial\tilde{\rho}}\phi &= \sum_c\sum_t L_\rho e^{-Rt}\Re\{K_{c,t}\} \\
\frac{\partial}{\partial\tilde{R}}\phi &= \sum_c\sum_t -L_R\rho te^{-Rt}\Re\{K_{c,t}\} \\
\frac{\partial}{\partial\tilde{b}}\phi &= \sum_c\sum_t L_b\rho e^{-Rt}\Re\{-i2\pi tK_{c,t}\} \\
\frac{\partial}{\partial\tilde{\varphi_0}}\phi &= \sum_c\sum_t L_{\varphi_0}\rho e^{-Rt}\Re\{-iK_{c,t}\} \\
K_{c,t} &= e^{-i(2\pi bt+\varphi_0)}\overline{C_c}\mathcal{F}^{-1}(Px_t(\rho,R,b,\varphi_0)C_c - y_{c,t})
\end{aligned} \tag{7.7}$$

# 7.2 Imaging Protocols

## 7.2.1 Two-Dimensional Gradient Recalled Echo

SIEMENS MAGNETOM TrioTim syngo MR B17

\\USER\ACIT\Tom\Tom_T2star_6.3.2013\t2star_2d-16_300mp_TEm=73_2mm

TA: 9:41 PAT: Off Voxel size: 1.1×1.1×2.0 mm Rel. SNR: 1.00 USER: gre_me

Properties

| | |
|---|---|
| Prio Recon | Off |
| Before measurement | |
| After measurement | |
| Load to viewer | On |
| Inline movie | Off |
| Auto store images | On |
| Load to stamp segments | Off |
| Load images to graphic segments | Off |
| Auto open inline display | Off |
| Start measurement without further preparation | On |
| Wait for user to start | Off |
| Start measurements | single |

Routine

| | |
|---|---|
| Slice group 1 | |
| Slices | 33 |
| Dist. factor | 0 % |
| Position | Isocenter |
| Orientation | Transversal |
| Phase enc. dir. | A >> P |
| Rotation | 0.00 deg |
| Phase oversampling | 0 % |
| FoV read | 204 mm |
| FoV phase | 100.0 % |
| Slice thickness | 2.0 mm |
| TR | 3000 ms |
| TE 1 | 4.35 ms |
| TE 2 | 8.94 ms |
| TE 3 | 13.53 ms |
| TE 4 | 18.12 ms |
| TE 5 | 22.71 ms |
| TE 6 | 27.3 ms |
| TE 7 | 31.89 ms |
| TE 8 | 36.48 ms |
| TE 9 | 41.07 ms |
| TE 10 | 45.66 ms |
| TE 11 | 50.25 ms |
| TE 12 | 54.84 ms |
| TE 13 | 59.43 ms |
| TE 14 | 64.02 ms |
| TE 15 | 68.61 ms |
| TE 16 | 73.20 ms |
| Averages | 1 |
| Concatenations | 1 |
| Filter | None |
| Coil elements | HEA;HEP |

Contrast

| | |
|---|---|
| MTC | Off |
| Magn. preparation | None |
| Flip angle | 90 deg |
| Fat suppr. | Fat sat. |
| Water suppr. | None |
| SWI | Off |
| Averaging mode | Short term |
| Reconstruction | Magn./Phase |
| Measurements | 1 |
| Multiple series | Each measurement |

Resolution

| | |
|---|---|
| Base resolution | 192 |
| Phase resolution | 100 % |
| Phase partial Fourier | Off |
| Interpolation | Off |
| PAT mode | None |
| Matrix Coil Mode | Auto (CP) |
| Image Filter | Off |
| Distortion Corr. | Off |
| Prescan Normalize | Off |
| Normalize | Off |
| B1 filter | Off |
| Raw filter | Off |
| Elliptical filter | Off |

Geometry

| | |
|---|---|
| Multi-slice mode | Interleaved |
| Series | Interleaved |
| Saturation mode | Standard |
| Special sat. | None |
| Set-n-Go Protocol | Off |
| Table position | H |
| Table position | 0 mm |
| Inline Composing | Off |
| Tim CT mode | Off |

System

| | |
|---|---|
| Body | Off |
| HEP | On |
| HEA | On |
| Positioning mode | REF |
| MSMA | S - C - T |
| Sagittal | R >> L |
| Coronal | A >> P |
| Transversal | F >> H |
| Save uncombined | Off |
| Coil Combine Mode | Sum of Squares |
| AutoAlign | Head > Basis |
| Auto Coil Select | Default |
| Shim mode | Standard |
| Adjust with body coil | Off |
| Confirm freq. adjustment | Off |
| Assume Silicone | Off |
| ? Ref. amplitude 1H | 0.000 V |
| Adjustment Tolerance | Auto |
| Adjust volume | |
| Position | Isocenter |
| Orientation | Transversal |
| Rotation | 0.00 deg |
| R >> L | 204 mm |
| A >> P | 204 mm |
| F >> H | 66 mm |

Physio

| | |
|---|---|
| 1st Signal/Mode | None |
| Segments | 1 |
| Tagging | None |
| Dark blood | Off |
| Resp. control | Off |

Inline

| | |
|---|---|
| Subtract | Off |

1/+

SIEMENS MAGNETOM TrioTim syngo MR B17

| | |
|---|---|
| Liver registration | Off |
| Std-Dev-Sag | Off |
| Std-Dev-Cor | Off |
| Std-Dev-Tra | Off |
| Std-Dev-Time | Off |
| MIP-Sag | Off |
| MIP-Cor | Off |
| MIP-Tra | Off |
| MIP-Time | Off |
| Save original images | On |
| Wash - In | Off |
| Wash - Out | Off |
| TTP | Off |
| PEI | Off |
| MIP - time | Off |
| MapIt | None |
| Contrasts | 16 |

Sequence

| | |
|---|---|
| Introduction | On |
| Dimension | 2D |
| Phase stabilisation | Off |
| Asymmetric echo | Off |
| Bandwidth 1 | 300 Hz/Px |
| Bandwidth 2 | 300 Hz/Px |
| Bandwidth 3 | 300 Hz/Px |
| Bandwidth 4 | 300 Hz/Px |
| Bandwidth 5 | 300 Hz/Px |
| Bandwidth 6 | 300 Hz/Px |
| Bandwidth 7 | 300 Hz/Px |
| Bandwidth 8 | 300 Hz/Px |
| Bandwidth 9 | 300 Hz/Px |
| Bandwidth 10 | 300 Hz/Px |
| Bandwidth 11 | 300 Hz/Px |
| Bandwidth 12 | 300 Hz/Px |
| Bandwidth 13 | 300 Hz/Px |
| Bandwidth 14 | 300 Hz/Px |
| Bandwidth 15 | 300 Hz/Px |
| Bandwidth 16 | 300 Hz/Px |
| Flow comp. 1 | No |
| Flow comp. 2 | No |
| Flow comp. 3 | No |
| Flow comp. 4 | No |
| Flow comp. 5 | No |
| Flow comp. 6 | No |
| Flow comp. 7 | No |
| Flow comp. 8 | No |
| Flow comp. 9 | No |
| Flow comp. 10 | No |
| Flow comp. 11 | No |
| Flow comp. 12 | No |
| Flow comp. 13 | No |
| Flow comp. 14 | No |
| Flow comp. 15 | No |
| Flow comp. 16 | No |
| Readout mode | Monopolar |
| Allowed delay | 0 s |
| RF pulse type | Normal |
| Gradient mode | Fast |
| Excitation | Slice-sel. |
| RF spoiling | On |
| Optimised MT | Off |
| MOSAIC Mode | Echoes |

## 7.2.2 Three-Dimensional Gradient Recalled Echo

SIEMENS MAGNETOM TrioTim syngo MR B17

\\USER\ACIT\Tom\Tom_T2star_6.3.2013\T2star_3D_

TA: 22:41 PAT: Off Voxel size: 1.6×1.6×1.6 mm Rel. SNR: 1.00 USER: gre_me

Properties

| | |
|---|---|
| Prio Recon | Off |
| Before measurement | |
| After measurement | |
| Load to viewer | On |
| Inline movie | Off |
| Auto store images | On |
| Load to stamp segments | Off |
| Load images to graphic segments | Off |
| Auto open inline display | Off |
| Start measurement without further preparation | On |
| Wait for user to start | Off |
| Start measurements | single |

Routine

| | |
|---|---|
| Slab group 1 | |
| Slabs | 1 |
| Dist. factor | 20 % |
| Position | L0.0 P5.9 F0.9 |
| Orientation | Sagittal |
| Phase enc. dir. | A >> P |
| Rotation | 0.00 deg |
| Phase oversampling | 0 % |
| Slice oversampling | 0.0 % |
| Slices per slab | 128 |
| FoV read | 204 mm |
| FoV phase | 100.0 % |
| Slice thickness | 1.60 mm |
| TR | 83 ms |
| TE 1 | 2.28 ms |
| TE 2 | 6.51 ms |
| TE 3 | 10.74 ms |
| TE 4 | 14.97 ms |
| TE 5 | 19.2 ms |
| TE 6 | 23.43 ms |
| TE 7 | 27.66 ms |
| TE 8 | 31.89 ms |
| TE 9 | 36.12 ms |
| TE 10 | 40.35 ms |
| TE 11 | 44.58 ms |
| TE 12 | 48.81 ms |
| TE 13 | 53.04 ms |
| TE 14 | 57.27 ms |
| TE 15 | 61.5 ms |
| TE 16 | 65.73 ms |
| Averages | 1 |
| Concatenations | 1 |
| Filter | None |
| Coil elements | HEA;HEP |

Contrast

| | |
|---|---|
| MTC | Off |
| Magn. preparation | None |
| Flip angle | 34 deg |
| Fat suppr. | Fat sat. |
| Water suppr. | None |
| SWI | Off |
| Averaging mode | Short term |
| Reconstruction | Magn./Phase |
| Measurements | 1 |
| Multiple series | Each measurement |

Resolution

| | |
|---|---|
| Base resolution | 128 |
| Phase resolution | 100 % |
| Slice resolution | 100 % |
| Phase partial Fourier | Off |
| Slice partial Fourier | Off |
| Interpolation | Off |
| PAT mode | None |
| Matrix Coil Mode | Auto (CP) |
| Image Filter | Off |
| Distortion Corr. | Off |
| Prescan Normalize | Off |
| Normalize | Off |
| B1 filter | Off |
| Raw filter | Off |
| Elliptical filter | Off |

Geometry

| | |
|---|---|
| Multi-slice mode | Interleaved |
| Series | Interleaved |
| Saturation mode | Standard |
| Special sat. | None |
| Set-n-Go Protocol | Off |
| Table position | H |
| Table position | 0 mm |
| Inline Composing | Off |
| Tim CT mode | Off |

System

| | |
|---|---|
| Body | Off |
| HEP | On |
| HEA | On |
| Positioning mode | REF |
| MSMA | S - C - T |
| Sagittal | R >> L |
| Coronal | A >> P |
| Transversal | F >> H |
| Save uncombined | Off |
| Coil Combine Mode | Sum of Squares |
| AutoAlign | Head > Basis |
| Auto Coil Select | Default |
| Shim mode | Standard |
| Adjust with body coil | Off |
| Confirm freq. adjustment | Off |
| Assume Silicone | Off |
| ? Ref. amplitude 1H | 0.000 V |
| Adjustment Tolerance | Auto |
| Adjust volume | |
| Position | L0.0 P5.9 F0.9 |
| Orientation | Sagittal |
| Rotation | 0.00 deg |
| F >> H | 204 mm |
| A >> P | 204 mm |
| R >> L | 205 mm |

Physio

| | |
|---|---|
| 1st Signal/Mode | None |
| Segments | 1 |
| Tagging | None |
| Dark blood | Off |

1/+

SIEMENS MAGNETOM TrioTim syngo MR B17

| | |
|---|---|
| Resp. control | Off |

Inline

| | |
|---|---|
| Subtract | Off |
| Liver registration | Off |
| Std-Dev-Sag | Off |
| Std-Dev-Cor | Off |
| Std-Dev-Tra | Off |
| Std-Dev-Time | Off |
| MIP-Sag | Off |
| MIP-Cor | Off |
| MIP-Tra | Off |
| MIP-Time | Off |
| Save original images | On |
| Wash - In | Off |
| Wash - Out | Off |
| TTP | Off |
| PEI | Off |
| MIP - time | Off |
| MapIt | None |
| Contrasts | 16 |

Sequence

| | |
|---|---|
| Introduction | On |
| Dimension | 3D |
| Elliptical scanning | Off |
| Phase stabilisation | Off |
| Asymmetric echo | Off |
| Bandwidth 1 | 300 Hz/Px |
| Bandwidth 2 | 300 Hz/Px |
| Bandwidth 3 | 300 Hz/Px |
| Bandwidth 4 | 300 Hz/Px |
| Bandwidth 5 | 300 Hz/Px |
| Bandwidth 6 | 300 Hz/Px |
| Bandwidth 7 | 300 Hz/Px |
| Bandwidth 8 | 300 Hz/Px |
| Bandwidth 9 | 300 Hz/Px |
| Bandwidth 10 | 300 Hz/Px |
| Bandwidth 11 | 300 Hz/Px |
| Bandwidth 12 | 300 Hz/Px |
| Bandwidth 13 | 300 Hz/Px |
| Bandwidth 14 | 300 Hz/Px |
| Bandwidth 15 | 300 Hz/Px |
| Bandwidth 16 | 300 Hz/Px |
| Flow comp. 1 | No |
| Flow comp. 2 | No |
| Flow comp. 3 | No |
| Flow comp. 4 | No |
| Flow comp. 5 | No |
| Flow comp. 6 | No |
| Flow comp. 7 | No |
| Flow comp. 8 | No |
| Flow comp. 9 | No |
| Flow comp. 10 | No |
| Flow comp. 11 | No |
| Flow comp. 12 | No |
| Flow comp. 13 | No |
| Flow comp. 14 | No |
| Flow comp. 15 | No |
| Flow comp. 16 | No |
| Readout mode | Monopolar |
| Allowed delay | 0 s |
| RF pulse type | Fast |
| Gradient mode | Fast |
| Excitation | Non-sel. |
| RF spoiling | On |
| Optimised MT | On |
| MOSAIC Mode | Echoes |

2/-

# Acronyms

**ADC** analogue-digital converter. 16

**ASL** arterial spin labelling. 11

**BOLD** blood oxygen level dependent. 28

**CG-descend** conjugate gradient descend. 22

**CHUV** Centre Hospitalier Universitaire Vaudois. 35

**CT** Computed Tomography. 11

**DTI** diffusion tensor imaging. 11

**FFT** Fast Fourier Transform. 57

**FFTW** "Fastest Fourier Transform in the West.". 36

**fMRI** functional MRI. 11

**FWHM** full-width-at-half-maximum. 57

**GESEPI** gradient-echo-slice-excitation-profile-imaging. 29

**GM** gray matter. 12

**GPU** Graphics Processing Unit. 57

**GRAPPA** Generalized Autocalibrating Partially Parallel Acquisitions. 11

**GRE** Gradient Recalled Echo. 12

**GSL** GNU Scientific Library. 36

**iFT** inverse Fourier transform. 16

**MRI** Magnetic Resonance Imaging. 11

**MRS** Spectroscopy. 11

**MSE** Multi-Spin Echo. 17

**NRMSE** normalized-root-mean-square-error. 36

**PCA** Principal Component Analysis. 37

**PSF** point-spread-function. 34

**RF** radio frequency. 14

**SENSE** Sensitivity Encoding. 11

**SNR** signal to noise ratio. 15

**SSIM** structural similarity measurement. 36

**TE** echo time. 17

**TGV** total generalized variation. 33

**TOF-MRA** time of flight angiography. 11

**TR** repetition time. 16

**TV** total variation. 32

**TV2** total variation of the second order. 32

**WM** white matter. 12

# Bibliography


[1] Kai Tobias Block, Martin Uecker, and Jens Frahm. Undersampled radial mri with multiple coils. iterative image reconstruction using a total variation constraint. *Magn Reson Med*, 57(6):1086–98, 2007.

[2] Kai Tobias Block, Martin Uecker, and Jens Frahm. Suppression of mri truncation artifacts using total variation constrained data extrapolation. *Int J Biomed Imaging*, 2008:184123, 2008.

[3] Kai Tobias Block, Martin Uecker, and Jens Frahm. Model-based iterative reconstruction for radial fast spin-echo mri. *IEEE Trans Med Imaging*, 28(11):1759–69, 2009.

[4] Martin Buehrer, Klaas P Pruessmann, Peter Boesiger, and Sebastian Kozerke. Array compression for mri with large coil arrays. *Magn Reson Med*, 57(6):1131–9, 2007.

[5] Z. H. Cho and Y. M. Ro. Reduction of susceptibility artifact in gradient-echo imaging. *Magnetic resonance in medicine*, 23(1):193–200, 1992.

[6] David Leigh Donoho. Compressed sensing. *Information Theory, IEEE Transactions on*, 52(4):1289–1306, 2006.

[7] Daniel Dunbar and Greg Humphreys. A spatial data structure for fast poisson-disk sample generation. In *ACM Transactions on Graphics (TOG)*, volume 25, pages 503–508, 2006.

[8] M. Galassi et al. *GNU Scientific Library Reference Manual (3rd Ed.)*.

[9] M. A. Fernández-Seara and F. W. Wehrli. Postprocessing technique to correct for background gradients in image-based r* 2 measurements. *Magnetic resonance in medicine*, 44(3):358–366, 2000.

[10] Jeffrey A. Fessler and W. Leslie Rogers. Spatial resolution properties of penalized-likelihood image reconstruction: space-invariant tomographs. *Image Processing, IEEE Transactions on*, 5(9):1346–1358, 1996.

[11] Jens Frahm, Klaus-Dietmar Merboldt, and Wolfgang Hänicke. Direct flash mr imaging of magnetic field inhomogeneities by gradient compensation. *Magnetic resonance in medicine*, 6(4):474–480, 2005.

[12] Matteo Frigo. A fast fourier transform compiler. In *Acm Sigplan Notices*, volume 34, pages 169–180, 1999.

[13] Amanda K Funai, Jeffrey A Fessler, Desmond T B Yeo, Valur T Olafsson, and Douglas C Noll. Regularized field map estimation in mri. *IEEE Trans Med Imaging*, 27(10):1484–94, 2008.

[14] D. Geman and C. Yang. Nonlinear image recovery with half-quadratic regularization. *Image Processing, IEEE Transactions on*, 4(7):932–946, 1995.

[15] Dennis C. Ghiglia and Louis A. Romero. Robust two-dimensional weighted and unweighted phase unwrapping that uses fast transforms and iterative methods. *JOSA A*, 11(1):107–117, 1994.

[16] Mark A Griswold, Peter M Jakob, Robin M Heidemann, Mathias Nittka, Vladimir Jellus, Jianmin Wang, Berthold Kiefer, and Axel Haase. Generalized autocalibrating partially parallel acquisitions (grappa). *Magn Reson Med*, 47(6):1202–10, 2002.

[17] E. Mark Haacke, Robert W. Brown, Michael R. Thompson, and Ramesh Venkatesan. *Magnetic resonance imaging: physical principles and sequence design*, volume 82. Wiley-Liss New York:, 1999.

[18] W. W. Hager and H. Zhang. A new conjugate gradient method with guaranteed descent and an efficient line search. *SIAM Journal on Optimization*, 16(1):170–192, 2005.

[19] Lili He and Nehal A. Parikh. Automated detection of white matter signal abnormality using t2 relaxometry: Application to brain segmentation on term mri in very preterm infants. *NeuroImage*, 64(0):328–340, 2013.

[20] Florian Knoll, Kristian Bredies, Thomas Pock, and Rudolf Stollberger. Second order total generalized variation (tgv) for mri. *Magn Reson Med*, 65(2):480–91, 2011.

[21] Florian Knoll, Christian Clason, Clemens Diwoky, and Rudolf Stollberger. Adapted random sampling patterns for accelerated mri. *MAGMA*, 24(1):43–50, 2011.

[22] M. Lustig, P. Lai, M. Murphy, S. M. Vasanawala, M. Elad, J. Zhang, and J. Pauly. An eigen-vector approach to autocalibrating parallel mri, where sense meets grappa. In *Proceedings of the 19th Annual Meeting of ISMRM, Montreal, QC, Canada*, page 479, 2011.

[23] Michael Lustig, David Donoho, and John M Pauly. Sparse mri: The application of compressed sensing for rapid mr imaging. *Magn Reson Med*, 58(6):1182–95, 2007.

[24] J.P. Marques and R. Bowtell. Application of a fourier-based method for rapid calculation of field inhomogeneity due to spatial variation of magnetic susceptibility. *Concepts in Magnetic Resonance Part B: Magnetic Resonance Engineering*, 25B(1):65, 2005.

[25] Donald W. McRobbie, Elizabeth A. Moore, Martin J. Graves, and Martin R. Prince. *MRI from Picture to Proton*. Cambridge University Press, 2002.

[26] J. C. Meza. Steepest descent. *Wiley Interdisciplinary Reviews: Computational Statistics*, 2(6):719–722, 2010.

[27] J. More. The levenberg-marquardt algorithm: implementation and theory. *Numerical analysis*, pages 105–116, 1978.

[28] Krishna S Nayak, Charles H Cunningham, Juan M Santos, and John M Pauly. Real-time cardiac mri at 3 tesla. *Magn Reson Med*, 51(4):655–60, 2004.

[29] Aaron Niebergall, Shuo Zhang, Martin Uecker, and Jens Frahm. Real-time mri of speaking: Preliminary experience at a temporal resolution of 33ms. 2012.

[30] Fabiana Novellino, Andrea Cherubini, Carmelina Chiriaco, Maurizio Morelli, Maria Salsone, Gennarina Arabia, and Aldo Quattrone. Brain iron deposition in essential tremor: A quantitative 3-tesla magnetic resonance imaging study. *Mov. Disord.*, 2012.

[31] Michael A Ohliger and Daniel K Sodickson. An introduction to coil array design for parallel mri. *NMR Biomed*, 19(3):300–15, 2006.

[32] Valur T Olafsson, Douglas C Noll, and Jeffrey A Fessler. Fast joint reconstruction of dynamic r2* and field maps in functional mri. *IEEE Trans Med Imaging*, 27(9):1177–88, 2008.

[33] K. P. Pruessmann, M. Weiger, M. B. Scheidegger, P. Boesiger, et al. Sense: sensitivity encoding for fast mri. *Magnetic Resonance in Medicine*, 42(5):952–962, 1999.

[34] L. I. Rudin, S. Osher, and E. Fatemi. Nonlinear total variation based noise removal algorithms. *Physica D: Nonlinear Phenomena*, 60(1):259–268, 1992.

[35] D. K. Sodickson and W. J. Manning. Simultaneous acquisition of spatial harmonics (smash): fast imaging with radiofrequency coil arrays. *Magnetic Resonance in Medicine*, 38(4):591–603, 2005.

[36] Henrik V. Sorensen and C. Sidney Burrus. Efficient computation of the dft with only a subset of input or output points. *Signal Processing, IEEE Transactions on*, 41(3):1184–1200, 1993.

[37] Tilman J Sumpf, Martin Uecker, Susann Boretius, and Jens Frahm. Model-based nonlinear inverse reconstruction for t2 mapping using highly undersampled spin-echo mri. *J Magn Reson Imaging*, 34(2):420–8, 2011.

[38] Martin Uecker, Thorsten Hohage, Kai Tobias Block, and Jens Frahm. Image reconstruction by regularized nonlinear inversion–joint estimation of coil sensitivities and image content. *Magn Reson Med*, 60(3):674–82, 2008.

[39] Gustav K von Schulthess and Cyrill Burger. Integrating imaging modalities: what makes sense from a workflow perspective? *Eur. J. Nucl. Med. Mol. Imaging*, 37(5):980–90, 2010.

[40] Z. Wang, A.C. Bovik, H.R. Sheikh, and E.P. Simoncelli. Image quality assessment: From error visibility to structural similarity. *IEEE Transactions on Image Processing*, 13(4):600, 2004.

[41] Janaka P. Wansapura, Scott K. Holland, R. Scott Dunn, and William S. Ball. Nmr relaxation times in the human brain at 3.0 tesla. *Journal of magnetic resonance imaging*, 9(4):531–538, 1999.

[42] M. Weiger, K. P. Pruessmann, C. Leussler, P. Röschmann, and P. Boesiger. Specific coil design for sense: A six-element cardiac array. *Magnetic resonance in medicine*, 45(3):495–504, 2001.

[43] L. A. Williams, N. Gelman, P. A. Picot, D. S. Lee, J. R. Ewing, V. K. Han, and R. T. Thompson. Neonatal brain: Regional variability of in vivo mr imaging relaxation rates at 3.0 t—initial experience1. *Radiology*, 235(2):595–603, 2005.

[44] Christian Windischberger, Simon Robinson, Alexander Rauscher, Markus Barth, and Ewald Moser. Robust field map generation using a triple-echo acquisition. *J Magn Reson Imaging*, 20(4):730–4, 2004.

[45] Dmitriy A Yablonskiy, Alexander L Sukstanskii, Jie Luo, and Xiaoqi Wang. Voxel spread function method for correction of magnetic field inhomogeneity effects in quantitative gradient-echo-based mri. *Magn Reson Med*, 2012.

[46] Qing X. Yang, Gerald D. Williams, Roger J. Demeure, Timothy J. Mosher, and Michael B. Smith. Removal of local field gradient artifacts in t2*-weighted images at high fields by gradient-echo slice excitation profile imaging. *Magnetic resonance in medicine*, 39(3):402–409, 1998.

[47] I. R. Young, I. J. Cox, D. J. Bryant, and G. M. Bydder. The benefits of increasing spatial resolution as a means of reducing artifacts due to field inhomogeneities. *Magnetic resonance imaging*, 6(5):585–590, 1988.

[48] Huanzhou Yu, Ann Shimakawa, Charles A McKenzie, Wenmiao Lu, Scott B Reeder, R Scott Hinks, and Jean H Brittain. Phase and amplitude correction for multi-echo water-fat separation with bipolar acquisitions. *J Magn Reson Imaging*, 31(5):1264–71, 2010.